



HAL
open science

HaloSat Observations of Heliospheric Solar Wind Charge Exchange

R. Ringuette, Dimitra Koutroumpa, K. D. Kuntz, P. Kaaret, K. Jahoda, D.
Larocca, M. Kounkel, J. Richardson, A. Zajczyk, J. Bluem

► **To cite this version:**

R. Ringuette, Dimitra Koutroumpa, K. D. Kuntz, P. Kaaret, K. Jahoda, et al.. HaloSat Observations of Heliospheric Solar Wind Charge Exchange. *The Astrophysical Journal*, 2021, 918 (2), pp.41. 10.3847/1538-4357/ac0e33 . insu-03338252

HAL Id: insu-03338252

<https://insu.hal.science/insu-03338252v1>

Submitted on 27 Sep 2024

HAL is a multi-disciplinary open access archive for the deposit and dissemination of scientific research documents, whether they are published or not. The documents may come from teaching and research institutions in France or abroad, or from public or private research centers.








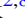

L'archive ouverte pluridisciplinaire **HAL**, est destinée au dépôt et à la diffusion de documents scientifiques de niveau recherche, publiés ou non, émanant des établissements d'enseignement et de recherche français ou étrangers, des laboratoires publics ou privés.



Distributed under a Creative Commons Attribution 4.0 International License



HaloSat Observations of Heliospheric Solar Wind Charge Exchange

R. Ringuette^{1,2} , D. Koutroumpa³ , K. D. Kuntz^{2,4} , P. Kaaret⁵ , K. Jahoda² , D. LaRocca⁶ , M. Kounkel⁷ ,
J. Richardson⁵ , A. Zajczyk^{2,8}, and J. Bluem⁵ 

¹ ADNET Systems, Inc., 6720 B Rockledge Dr., Suite 504, Bethesda, MD 20817, USA; rebecca.ringuette@nasa.gov

² NASA Goddard Space Flight Center, Greenbelt, MD 20771, USA

³ LATMOS/IPSL, CNRS, UVSQ Paris-Saclay, Sorbonne Université, Guyancourt, France

⁴ The Henry A. Rowland Department of Physics and Astronomy, Johns Hopkins University, Baltimore, MD 21218, USA

⁵ Department of Physics and Astronomy, University of Iowa, Van Allen Hall, Iowa City, IA 52242, USA

⁶ Department of Astronomy and Astrophysics, 525 Davey Lab, Pennsylvania State University, University Park, PA 16802, USA

⁷ Department of Physics and Astronomy, Western Washington University, 516 High St., Bellingham, WA 98225, USA

⁸ Center for Space Sciences and Technology, University of Maryland, Baltimore County, 1000 Hilltop Circle, Baltimore, MD 21250, USA

Received 2020 October 16; revised 2021 June 8; accepted 2021 June 22; published 2021 September 6

Abstract

X-ray emission from solar wind charge exchange (SWCX) produced in interplanetary space contaminates every astrophysical observation, regardless of the line of sight. Unfortunately, the primary SWCX emission lines also happen to be important diagnostics of astrophysical plasmas. Models of SWCX emission are limited by two main uncertainties: the local solar wind fluxes along the line of sight and the charge exchange cross sections. The He cone, a localized density enhancement of helium neutrals, is the only heliospheric SWCX emission feature that is small enough and bright enough to be observationally isolated from the X-ray background and the broader SWCX emission. HaloSat, an X-ray CubeSat mission, has recently completed two series of specialized observations, near and far from the ecliptic plane, during two Earth transits of the He cone. These observations were used to test the predictions of an SWCX emission model against the emission observed at low ecliptic latitude, where the solar wind data are monitored, and at high ecliptic latitude, where the solar wind data are extrapolated. The measured SWCX emission for the set of observations near the ecliptic plane was consistent with the line intensities predicted by the model but underpredicted for the set of observations at high ecliptic latitude near the south ecliptic pole. Additionally, high-temperature Galactic halo emission components are reported for both spectral sets.

Unified Astronomy Thesaurus concepts: Diffuse x-ray background (384); Solar wind (1534); Charge exchange ionization (2056); Milky Way dark matter halo (1049)

1. Introduction

Solar wind charge exchange (SWCX) emission is a relative newcomer to astrophysics. When soft X-ray observations of comets revealed them to be far brighter than expected (Lisse et al. 1996), charge exchange between the cometary neutrals and solar wind ions was proposed as the emission mechanism (Cravens 1997). It was soon realized that the “long-term enhancements” (LTEs) observed in the ROSAT All-Sky Survey (RASS) data were due to the solar wind interaction with the Earth’s exosphere (Freyberg 1994, 1998; Cravens et al. 2001). The LTEs were periods of enhanced X-ray background with timescales of hours to days and thought to originate in cis-lunar space, since the X-ray emission toward the dark side of the moon was consistent with the contemporary LTE rate (Schmitt et al. 1991). Cox (1998) suggested that if the exosphere were a source of X-ray emission, then the neutral interstellar medium (ISM) flowing through the heliosphere should be absolutely glowing in soft X-rays.

This SWCX emission placed severe constraints on the extent to which one could study extended diffuse emission; no part of the sky could be observed without looking through the poorly understood and almost completely uncharacterized SWCX emission. (For a more complete discussion of the problems posed to astrophysics by SWCX emission, see Kuntz 2018.) Further, there are at least two different components to the SWCX emission: that due to the compressed solar wind in the magnetosheath interacting with the exosphere, and that due to the free-flowing solar wind interacting with the neutral ISM

within the entire heliosphere (radius ~ 100 au). The former can be avoided with special observing strategies that are generally not available to current X-ray observatories, while the latter is ubiquitous.

The SWCX emission is particularly problematic for astrophysical observations due to its spectrum. The SWCX emission is in lines, some of which are the same lines that are used to diagnose astrophysical plasmas. Thus, unrecognized SWCX emission can significantly modify the measured plasma temperature or be mistaken as a completely separate astrophysical component. (Consider, for example, the controversy over the existence of the Local Hot Bubble, LHB.) As the implications of SWCX for X-ray astrophysics, and particularly X-ray spectroscopy, became clearer, a number of groups began to explore the possibilities of characterizing the SWCX emission as a function of direction and time. This work is a test of our current capability to model the heliospheric emission.

The SWCX emission along the line of sight depends upon the ion and neutral densities, whether exospheric or interplanetary, along the line of sight; the relative velocities of the neutrals and ions; and the interaction cross sections. The poor state of the required atomic data in the relevant energy range was immediately noted; few species had measured interaction cross sections at energies of a fraction to a few keV amu^{-1} . This work will be primarily concerned with charge exchange due to Ne^{+9} , O^{+8} , and O^{+7} for several reasons: charge exchange of neutrals with these ions produces the most prominent SWCX spectral lines in the energy range of current X-ray instruments,

reasonably good cross sections have been established (Table 1 in Koutroumpa et al. 2006 and references therein), and there is solar wind monitoring to provide abundances.

The neutral ISM within the heliosphere has been an active topic of research for many years (e.g., Fahr 1968; Lallement et al. 1985; Katushkina & Izmodenov 2010), and the models of the neutral distribution have been observationally tested by backscattered Ly- α photons by Prognoz (Bertaux et al. 1985) and Solar Wind ANisotropies (SWAN; Bertaux et al. 1997; Quémerais et al. 1999; Lallement et al. 2004), He I 584 Å backscatter (e.g., Dalaudier et al. 1984; Möbius et al. 2004), direct detection of neutral ISM He (Witte et al. 1996; Möbius et al. 2004), energetic neutral atoms (ENAs; Hilchenbach et al. 1998; Czechowski et al. 2004, 2006; Bzowski 2008; Schwadron & McComas 2010), and H and He pickup ions (Möbius et al. 1985; Burlaga et al. 1996; Gloeckler 1996; Gloeckler et al. 1998; Möbius et al. 2004). Thus, the interplanetary neutral distribution is well understood and observationally confirmed by multiple different means.

The solar wind ion distribution is far more problematic. It is understood that during solar minimum (roughly the time with which this study is concerned), the quiescent solar wind is bimodal. In an oversimplification that we will also employ here, the two flows are named “slow” and “fast.” However, the fast and slow solar winds are defined more by their ion abundance ratios and temperatures than by their velocities (e.g., see review by von Steiger 2008). Within the solar equatorial flow, the solar wind speed is low, the solar wind density is high, and the high-state ions that produce the X-ray emission tend to have higher relative abundances. Within the solar polar flow, the solar wind speed is high, the solar wind density is low, and the high-state ions tend to have lower relative abundances. The division between the equatorial and polar flows tends to be at a solar latitude of 15°–20°. Due to the many upwind solar wind probes at Earth’s L1 point, as well as the rotation of the Sun, the equatorial flow is continuously sampled, and one can, with some complex interpolation, reconstruct, however roughly, the solar wind conditions along a line of sight within the equatorial flow. The polar flow, however, though studied over more than a solar cycle by Ulysses, is not currently monitored by the direct sampling required to determine abundances or ionization states; one can only assume that it has, in general, the mean properties measured by Ulysses. The polar flow is, however, monitored by indirect methods (e.g., full-sky maps of the backscattered Ly- α or interplanetary scintillation) that provide only averages of the solar wind speed and density over Carrington rotation scales (Koutroumpa et al. 2019; Sokół et al. 2020).

One could imagine testing a model of the heliospheric emission through the study of either spatial or temporal variation of the emission. There are two major components to the heliospheric emission: that due to charge exchange with neutral H and that due to charge exchange with neutral He. Figure 1 shows the relative density distribution of the neutral H and He due to the flow of the ISM. The distribution is shown within the ecliptic plane, which is entirely within the solar equatorial flow. The H is mostly ionized in the inner solar system (mostly by charge exchange with solar wind protons but with some photoionization as well), and the remaining H provides only a low amplitude variation with ecliptic longitude. The He, however, is neither strongly photoionized nor strongly ionized by charge exchange and is gravitationally focused by

the Sun. Since the ISM flow is in the ecliptic direction ($\lambda, \beta = (74^\circ.7, -5^\circ.3)$), the He cone is roughly in the plane of the ecliptic and the region dominated by the solar equatorial flow. In December, when the Earth is in the He cone, one would expect an observation along the cone to produce a very strong X-ray signal. That signal was seen in the broad $\frac{1}{4}$ keV X-ray band with the DXL sounding rocket flight (Galeazzi et al. 2014; Uprety et al. 2016). Because that measurement was made over a roughly 5 minute observation, temporal effects were minimized. A subsequent DXL flight measured the location and width of the peak of the X-ray signal and found that both are consistent with He neutral density models. Thus, our heliospheric emission model has been tested against the expected spatial distribution of emission. Since the test was done in the broad $\frac{1}{4}$ keV X-ray band, which has many lines from many different species, it is difficult to determine whether the amplitude of the emission is correct; indeed, the observations were done in order to determine the production factor for SWCX with He in that band in order to determine how much SWCX emission might remain in the RASS. Testing the spatial variation of the emission due to the distribution of interstellar H is more problematic given the lower amplitude, larger angular scale variation.

In this work, we turn our attention to tests more strongly dominated by the temporal variation of the heliospheric emission. Given that we know that the He cone does produce a strong heliospheric SWCX signal, it is an ideal target for measuring the temporal variation of the SWCX. If one takes a series of observations along the He cone as the Earth moves through it, there will be temporal variations due to both the motion of the Earth through the cone and the temporal variation of the solar wind. From the robust models of the interplanetary neutral He distribution and the DXL observations, the spatial variation should be well understood, allowing one to test the response of the model to variations in the solar wind. The He cone is also ideal in the sense that it lies within the solar equatorial flow for which we have continuous monitoring at L1. Of course, the solar wind along our line of sight is not directly monitored, but we may use simple assumptions together with the L1 monitoring to create a relatively robust model of the solar wind along the line of sight. We can then compare our model of the heliospheric emission along our line of sight down the length of the He cone with the observations.

From the above precis of the solar wind, we would expect a model of the heliospheric emission to be more secure for a line of sight that is totally within the solar equatorial flow, simply because we have more information about the solar wind in that region. However, we can make an initial comparison of our heliospheric emission model at high solar latitudes by observing perpendicular to the ecliptic. As can be seen from Figure 3, to observe perpendicular to the ecliptic plane, one must observe at the solstice for the pole of choice, either December for the ecliptic south pole (ESP) or June for the ecliptic north pole (ENP), in order to avoid strong magnetospheric SWCX emission associated with the extended cusp region. As the Earth passes through the He cone, it passes over (to the north of) the core of the He cone, so an observation of the ESP will pass through the core of the cone. As can be seen from Figure 2, we expect 75% of the heliospheric SWCX signal to arise from the closest 0.5 au of the line of sight and the remainder of the signal to arise from the heliospheric SWCX due to the solar polar flow. As with observations down the He

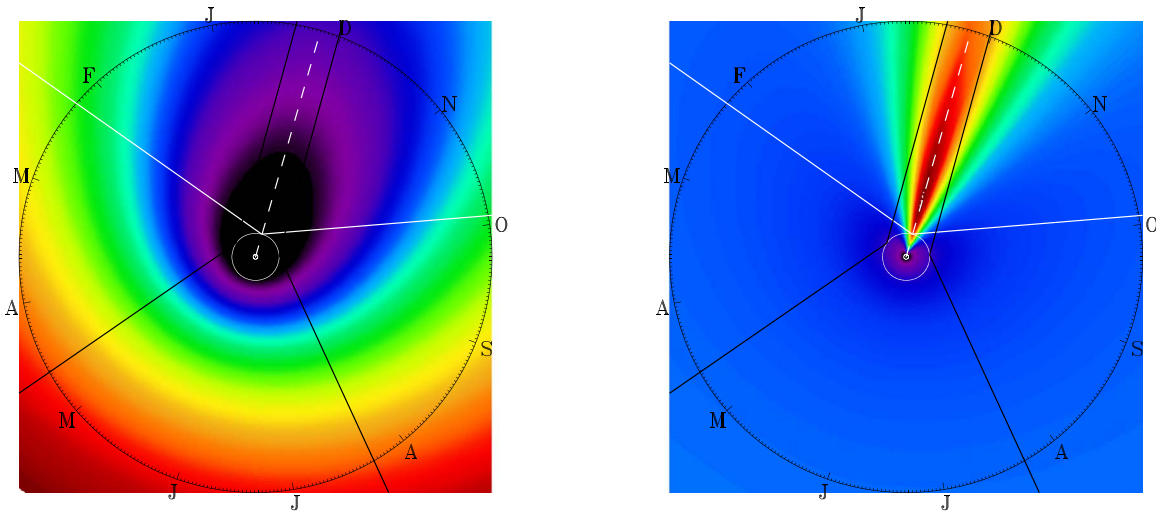


Figure 1. Distribution of neutral H (left) and He (right) in the ecliptic plane. The linear scale runs from black (minimum density) through purple to red (maximum density). The orbit of the Earth about the Sun has been marked (small white circle), as has the part of the sky observable by HaloSat on December 7 (solid white lines) and ± 71 days (solid black lines), the interval for which the He cone is observable by HaloSat. Our observations were made parallel to the dashed white lines. At the ± 71 day locations, observations of the He cone will necessarily be through part of the magnetosheath. The outer ring has a radius of 10 au and has been marked to show the angular location of the Earth at the beginning of each month.

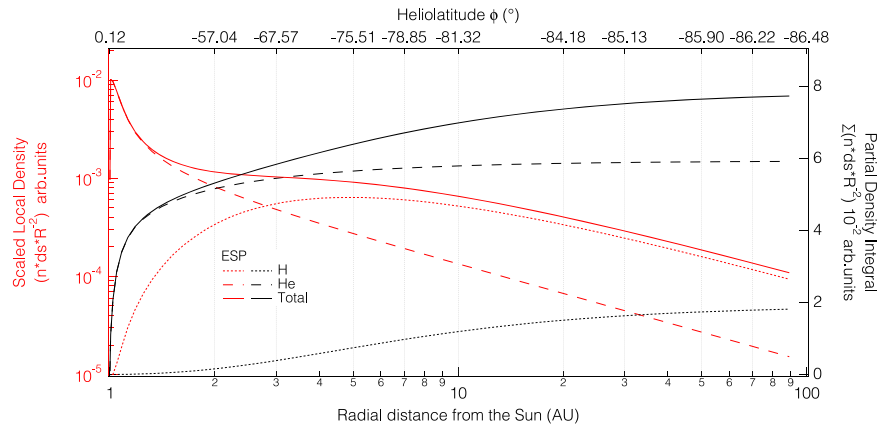


Figure 2. Qualitative function/distribution of the heliospheric SWCX emission due to charge exchange with H (dotted lines), He (dashed lines), and their total emission (solid lines) for the ESP. In red (left axis in logarithmic scale) are shown the neutral density profiles, scaled to the R^{-2} radial distance to account for the dilution of solar wind and the spatial step (ds) along the line of sight of the heliospheric simulations. In black (right axis in linear scale) are shown the partial density integrals along the line of sight, which are proportional to the SWCX emission assuming a uniform solar wind (see Section 3.1 for the heliospheric model description and details).

cone, temporal variation of the SWCX emission will be due to both the motion of the Earth with respect to the He cone and the variation of the solar wind. If the model used to determine the temporal variation for observations along the He cone is consistent with observations, then it can be used to model that part of the emission, allowing us to isolate the emission due to the high solar latitude emission.

Observations of the temporospatial variation of the SWCX emission have been attempted in the past with XMM-Newton and Suzaku. However, their small fields of view, limited temporal coverage, and severely constrained observing geometries make such observations difficult. Most astrophysical observatories, for example, are constrained to observe nearly perpendicular to the Earth–Sun line and thus cannot observe down the He cone. Both XMM-Newton and Suzaku have observed the ESP as the Earth passed through the cone but with equivocal results (Koutroumpa et al. 2009). With a 10° circular field of view, HaloSat has a grasp of $17.6 \text{ cm}^2 \text{ deg}^2$,

comparable to that of Suzaku ($18.4 \text{ cm}^2 \text{ deg}^2$), though \sim four times smaller than that of XMM-Newton. HaloSat is generally constrained to observe within 70° of the anti-Sun direction in order to avoid the SWCX emission from the flanks of the Earth’s magnetosheath, but exceptions are made for fields at higher ecliptic latitude.

This work presents a series of observations made by HaloSat along the He cone in 2018 and 2019, during solar minimum, for a study of the temporal variation of the SWCX emission. Due to the observing geometry, one cannot observe the diffuse X-ray background in this direction without at least some contribution from the He cone. Thus, we will detail a rather complex process by which we disentangle the cosmic and heliospheric emission components, essentially assuming that averaging the SWCX emission model over all of the observations provides an adequate representation of the mean observation and then looking at the deviation from the mean for each observation. We also describe a second, shorter series of

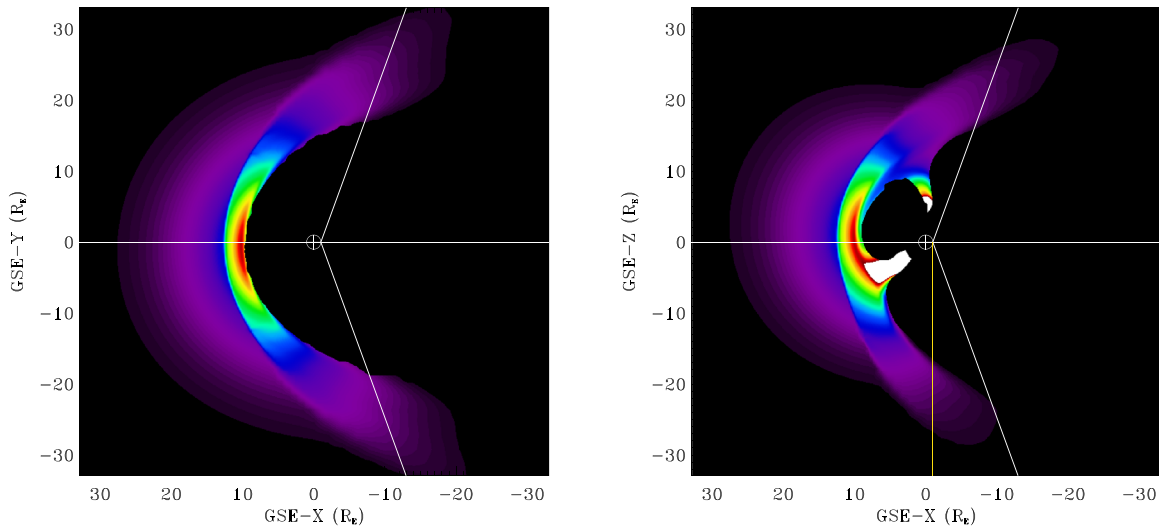


Figure 3. Cross section of a model of the X-ray emissivity in the magnetosheath due to SWCX. On the left is a cut in the ecliptic plane, while on the right is a cut in the noon–midnight plane. The linear scale runs from black (minimum density) through purple to red and white (maximum density). The MHD model used for this illustration was BATS-R-US (Tóth et al. 2005) for 2018 December 3, when the solar wind pressure was 1.96 nPa. The direction in which HaloSat could observe with only a marginal magnetospheric contribution is marked (angled white lines), as is the direction of the ESP (yellow line). Note that the ESP lies outside of the usual HaloSat observing window.

observations made of the ESP viewed through the He cone that provides a test of our heliospheric SWCX emission model at higher solar latitudes.

The following section provides details concerning the HaloSat instrument, observing strategy, and data preparation. Next, Section 3 describes the heliospheric SWCX emission model, how that model is incorporated as a spectral model, and how the other spectral components are modeled. The spectral fitting procedure and related simulation are detailed in Section 4. Finally, the results of the Galactic halo analysis are discussed in Section 5, with the performance results of the heliospheric models discussed in Section 6 and concluding remarks in Section 7.

2. Data Selection and Preparation

HaloSat is a nonimaging X-ray spectrometer housed on a 6U CubeSat platform with approximate dimensions of $10 \times 20 \times 34$ cm in low Earth orbit (LaRocca et al. 2020). Due to advantageous design choices, the instrument collected data for approximately 2 yr, longer than most other CubeSat missions, entering the Earth’s atmosphere in 2021 January. During flight, its three silicon drift detectors collected photons from almost identical circular areas on the sky (fields of view) with a diameter of 14° when projected onto the celestial coordinate sphere. Each detector responded uniformly to any radiation in the central 10° of the field of view, with the response decreasing linearly to zero toward the edges (at a diameter of 14° ; Kaaret et al. 2019).

HaloSat’s spectral resolution varies over its 0.4–7 keV energy range. Given HaloSat’s science goal to map emission from the O VII line in soft X-rays, the instrument was designed to have an energy resolution better than 100 near 600 eV. Specifically, Zajczyk et al. (2020) reported HaloSat’s energy resolution to be ≈ 85 at 676.8 eV with no significant difference between the energy calibrations of the three individual silicon drift detectors.

Two approximately perpendicular lines of sight were chosen for this study. The general direction of the low ecliptic latitude

(ECL) field of view (ECL) was selected to maximize the path length through the high-density portion of the He cone (see Figure 1). The ESP field of view was included in the analysis in order to test the impact of the latitudinal distribution of the slow and fast solar wind regimes on the SWCX line intensity. In both cases, the exact coordinates of each field were chosen to avoid the bright point sources found in the ROSAT, Uhuru, and MAXI catalogs, including the Large Magellanic Cloud near the ESP.

HaloSat’s observational constraints limited the times in which the desired observations were allowed. The instrument only observed at Sun angles greater than 110° to minimize contribution from magnetospheric SWCX. Additionally, HaloSat only observed on the nightside of each ~ 90 minute orbit to conserve power and minimize temperature fluctuations during observations. Observations along the He cone (ECL) obey these observing constraints from October through February of each year, as shown in Figure 1, and those observations are free of SWCX emission from the magnetosheath. There may be some SWCX contribution from the magnetotail, but, as argued in Kuntz (2018, see Section 10.1.1), that contribution is at least an order of magnitude lower than that from the flanks of the magnetosheath. The ECL observations in September or March require somewhat smaller Sun angles than the constraint allows and thus may be observed through the outer flanks of the magnetosheath. Thus, these observations may contain magnetospheric SWCX emission. It was also not possible to obey the Sun angle constraint for the ESP observations, as shown by the yellow line in Figure 3, so the ESP observations may also contain magnetospheric SWCX emission. The amount of magnetosheath emission in those observations will be discussed further in a later section.

After commissioning in 2018 October, monthly observations were attempted for ± 3 months of Earth’s transit of the He cone in 2018 and 2019 December. Each observation contains emission from the astrophysical X-ray background. Given the lack of bright sources in the chosen fields of view, the large areas of each field of view, and the short timescale over which the data were acquired (as compared to cosmic timescales), the

astrophysical X-ray background for each field of view is considered invariant. Each observation also contains the time-variable heliospheric SWCX emission, and possibly some SWCX emission due to the magnetosheath, with all emission lines located below 2 keV. However, the detectors also record a signal due to highly charged particles. These particles may interact directly with the detector or the materials around the detector, producing X-rays or secondary particles that are recorded by the detector. This “particle background” or “instrumental background” is time variable and usually seen as fluorescence lines and a power-law continuum in the spectrum. Thus, variations in the count rate above 3 keV cannot be attributed to either SWCX emission lines, instrumental fluorescence lines, or astrophysical background but are instead due to the particle background.

Periods in which the particle background is large compared to the astrophysical X-ray background were removed. The data were binned in 64 s bins, and those bins with count rates above $0.12 \text{ count s}^{-1}$ in the 3–7 keV band and $0.75 \text{ count s}^{-1}$ in the $>7 \text{ keV}$ band were removed. Then, the remaining intervals of good data were combined into groups called observations if the intervals occurred within 24 hr of other good intervals for the same target. Observations with at least 90% of the observing time removed by cleaning cuts or with less than 5 ks left per detector for more than one detector were also removed from further analysis.

As noted, the ESP could only be observed through the flanks of the Earth’s magnetosheath. Similarly, observations of the ECL field of view taken ± 3 months from the transit of the He cone were taken through the magnetosheath. So, we further filter the data to exclude observations taken of either target with average solar wind proton fluxes above $4 \times 10^8 \text{ protons cm}^{-2} \text{ s}^{-1}$ (Yoshino et al. 2009) as extracted from NASA/GSFC’s OMNI data set through OMNIWeb (King & Papitashvili 2005). This excludes one of the observations of the ESP, specifically the Dec2019a observation, but none of the ECL observations. Given the short instrument lifetime compared to the solar cycle, the restricted months during which observations of these targets were possible, and the background noise levels during each observation, we had no opportunity to explore the effects of the variation of the type of solar wind in any systematic way.

Despite strict data cleaning, some residual particle background will remain in the observations. Due to the spectral shape of the particle background, residual contamination is indicated by simultaneous increases in the count rates of high- and low-energy bands, with an approximately constant ratio between the count rates. However, inspecting the ratio of the average count rate per orbit in a band containing the oxygen lines, 0.45–0.73 keV, and a higher-energy band, 3–7 keV, showed that all variations were within the error bars (not shown). On the other hand, comparing the count rates in the same energy bands for the individual observations (Figure 4) shows a roughly linear relation between the two bands, indicating that some local particle contamination remains in the cleaned observations. The $(0.45\text{--}0.73 \text{ keV})/(3\text{--}7 \text{ keV})$ band ratios for the individual observations do not show significant variation from the mean $(0.45\text{--}0.73 \text{ keV})/(3\text{--}7 \text{ keV})$ band ratio.

The remaining observations are listed in Table 1, with observation names, start and end times given in UTC, the average angle between the pointing direction and the Sun given with the standard deviation, and the exposure time remaining

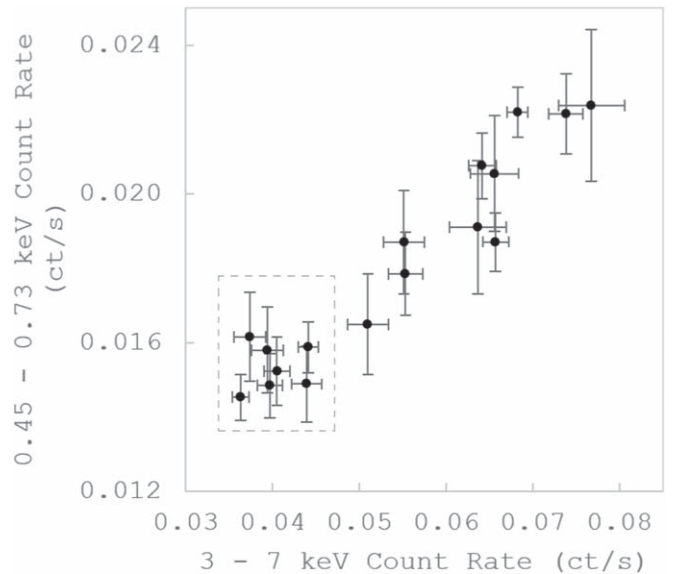


Figure 4. Count rate comparison per observation. Error bars show 1σ errors. Only data for the ECL target are shown. The dashed box encloses the observations considered to have low backgrounds, as described in the text.

after data cleaning in kiloseconds. The observation names consist of the first three letters of the month name combined with the four-digit year in which the observation was taken, with additional letters as needed to distinguish between observations taken of the same target in the same month. The observation details of the ECL target are given in the top portion of the table, with the ESP observations in the bottom portion. The Galactic coordinates of each field of view are given in the table note.

Observations of the ECL field of view were affected by an offset issue in 2018 October and November, as described in Kaaret et al. (2019), resulting in four additional target coordinates within 1° of the intended coordinates ($l, b = 182^\circ.7, -16^\circ.4$). Later observations were taken of one of these targets for comparison with the intended target, but no significant differences were noted. Therefore, no distinction is made between the observations taken at offset coordinates and the intended coordinates.

As shown by the dashed box in Figure 4, cleaned observations with high-energy count rates below $0.05 \text{ count s}^{-1}$ were considered low-background observations and are indicated by the italicized observation names in Table 1. Coincidentally, this requirement also excludes the ECL observations taken through the magnetosheath. Although not shown in Figure 4, four out of the six cleaned observations of the ESP with low solar wind proton fluxes were low-background observations by the same criteria. Summarizing, 47% of the 1120.4 ks of cleaned observing time of the ECL target shown in Figure 4 had higher particle backgrounds, as shown by the markers outside of the dashed box, with none lost to high solar wind proton fluxes. Out of 268.8 ks of cleaned observing time of the ESP target, 9% was removed due to high solar wind proton fluxes, and 54% had higher particle backgrounds. While only low-background observations were used in the first stage of the analysis described in the sections below, the other cleaned observations listed in Table 1 were included in the second stage of the analysis as possible, including the Dec2019a observation of the ESP.

Table 1
Observations during HaloSat’s He Cone Transits

Observation	Start Time (UTC) ^a	End Time (UTC) ^a	Sun Angle	Exposure (ks)
Oct2018a	2018/10/17 05:28	2018/10/18 11:09	128°9 ± 0°2	17.6
Oct2018b	2018/10/19 19:12	2018/10/21 00:56	131°4 ± 0°2	43.1
Nov2018a	2018/11/14 12:17	2018/11/15 02:15	158°6 ± 0°1	29.1
<i>Nov2018b</i>	2018/11/17 17:25	2018/11/18 07:41	161°5 ± 0°1	35.2
Dec2018a	2018/12/02 11:42	2018/12/07 13:51	174°1 ± 0°3	143.8
Dec2018b	2018/12/08 21:51	2018/12/11 10:19	173°2 ± 0°2	57.4
Feb2019	2019/02/05 08:34	2019/02/05 22:49	117°1 ± 0°1	25.0
Mar2019	2019/03/04 07:43	2019/03/04 21:57	90°4 ± 0°1	16.0
Sep2019	2019/09/15 13:03	2019/09/16 12:26	99°1 ± 0°1	43.4
Oct2019	2019/10/15 05:48	2019/10/17 05:35	127°6 ± 0°3	101.6
Nov2019a	2019/11/09 19:28	2019/11/10 11:12	153°6 ± 0°1	34.2
Nov2019b	2019/11/14 22:14	2019/11/15 21:38	158°2 ± 0°2	53.4
Nov2019c	2019/11/16 23:20	2019/11/17 22:43	160°0 ± 0°2	59.6
<i>Dec2019</i>	2019/12/04 08:01	2019/12/09 09:30	175°1 ± 0°1	266.2
Jan2020	2020/01/05 00:33	2020/01/07 00:27	148°2 ± 0°4	78.2
Feb2020	2020/01/31 13:47	2020/02/02 13:41	121°3 ± 0°3	89.9
Mar2020	2020/02/29 03:53	2020/02/29 15:00	93°9 ± 0°1	26.8
Dec2018a	2018/12/03 03:29	2018/12/03 17:45	92°26 ± 0°01	20.1
Dec2018b	2018/12/05 01:43	2018/12/10 19:11	92°6 ± 0°1	134.7
<i>Dec2019a^b</i>	2019/12/04 08:21	2019/12/05 07:42	92°04 ± 0°02	24.7
Dec2019b	2019/12/06 09:25	2019/12/07 08:48	92°54 ± 0°02	19.4
Dec2019c	2019/12/08 10:30	2019/12/09 09:54	92°97 ± 0°02	15.4
Dec2019d	2019/12/29 21:35	2019/12/30 20:49	94°78 ± 0°01	44.6
Feb2020	2020/02/25 01:57	2020/02/26 01:19	96°487 ± 0°002	28.0

Notes. Italicized observation names indicate observations with very low background; bold observation names indicate data included in the composite spectrum for each target. Top: ECL observations ($l, b = 182^\circ 7, -16^\circ 4$). Bottom: ESP observations ($l, b = 271^\circ 2, -24^\circ 0$).

^a Dates and times given with year, month, and day, followed by the time in UTC in hours and minutes.

^b The average solar wind proton flux for the Dec2019a observation after data cleaning was 4.19×10^8 protons $\text{cm}^{-2} \text{s}^{-1}$.

3. Spectral Model

The spectral model for each field of view consists of three general categories: the heliospheric SWCX emission, astrophysical emission, and the particle background. The unique capability of the heliospheric SWCX model presented in the following section is to predict the amount of heliospheric SWCX emission in a given observation. Although we have modeled all of the major SWCX species in HaloSat’s energy range, we will find we only have a sufficient signal-to-noise ratio to compare the predicted O VII line intensity to that observed. We have no way of assessing the relative strengths of different SWCX lines in the spectra. The calculation of the heliospheric SWCX emission for each observation is explained in the next section, followed by our method to include the calculation results in the spectral model. Finally, we outline our choices to model the astrophysical and particle backgrounds.

3.1. Heliospheric SWCX Calculation

The predicted X-ray line intensity I in line units ($\text{LU} = \text{ph cm}^{-2} \text{s}^{-1} \text{sr}^{-1}$) for each spectral line γ in HaloSat’s energy range in each observation was calculated using the same three-dimensional models used by Kaaret et al. (2020). As in that work, the calculation also takes into account the instrument’s field of view. The H and He neutral distributions, N_{H} and N_{He} , as a function of ecliptic longitude λ , latitude β , and distance from the Sun R , were calculated as a function of the solar conditions at the time of observation, particularly the latitude-dependent solar wind speeds and densities projected to each position along the line of sight (Koutroumpa et al. 2006;

Koutroumpa 2012). The ion density along the line of sight was derived from the Advanced Composition Explorer (ACE) Solar Wind Ion Composition Spectrometer (SWICS; Gloeckler et al. 1998) data acquired when ACE was properly positioned for the observation in question. As in Kaaret et al. (2020), we assume that the ACE measurements are valid for the HaloSat exposures within the longitudinal quarter of the sky around the Earth’s/ACE position on the date of each exposure. Then we calculate the propagation time according to the solar wind speed recorded at ACE and apply the relevant ACE data set along the corresponding portion of the HaloSat line of sight. (See Koutroumpa 2012 and Kaaret et al. 2020 for more details.) The velocity-dependent cross sections, σ , and photon yields, Y , for the primary ion species in our energy band are relatively well understood (Koutroumpa et al. 2007). From Kaaret et al. (2020), we find

$$I_{\gamma} = \frac{1}{4\pi} \sum_{j=1}^N F_{Xq+}(\lambda_j, \beta_j, R_j) \times [N_{\text{H}}(\lambda_j, \beta_j, R_j) \sigma_{\text{H},Xq+} Y_{\gamma,\text{H}} + N_{\text{He}}(\lambda_j, \beta_j, R_j) \sigma_{\text{He},Xq+} Y_{\gamma,\text{He}}] ds, \quad (1)$$

where the sum is over the increments j along the line of sight. Here $F_{Xq+}(\lambda_j, \beta_j, R_j)$ is the value of the flux of the ion, $Xq+$, at each location contributing to the observed spectral line γ . The ion may charge-exchange with either neutral H or neutral He, for which the cross sections and photon yields are different. The combinations of these differing charge exchange interactions are multiplied by the flux of the ion at each location before summing.

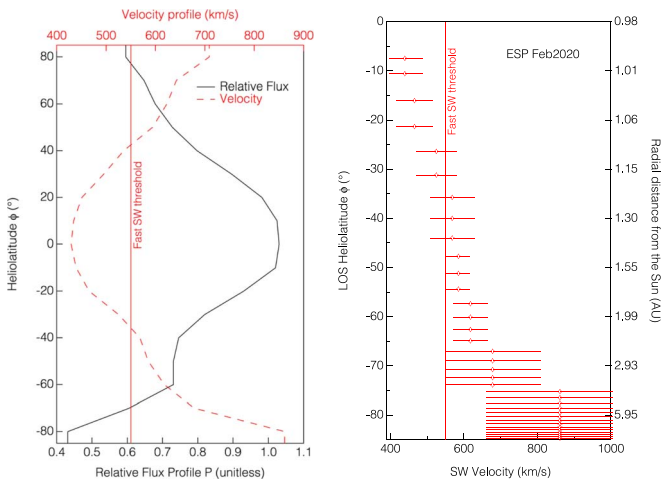


Figure 5. Solar wind flux and velocity profiles. Left: average solar wind proton flux helioclatitude profile in 10° bins relative to the equatorial value (black curve) for the solar minimum period (2018–2020) derived from the SOHO/SWAN full-sky hydrogen Ly α map inversion analysis (Koutroumpa et al. 2019) and average solar wind velocity helioclatitude profile (red dashed curve) derived from the same analysis. The red vertical line represents the fast solar wind threshold at 550 km s^{-1} used to determine the cross sections’ dependence over latitude. Right: local solar wind velocity helioclatitude profile along the line of sight of the Feb2020 observation of the ESP, derived from the profile in the left panel. The local helioclatitude of each step is marked on the left axis, with the corresponding radial distance from the Sun marked on the right axis. The red vertical line represents the fast solar wind threshold at 550 km s^{-1} .

The same empirical models for the O^{7+} and O^{8+} fluxes were used as in Kaaret et al. (2020), with an additional empirical relation for Ne^{9+} , which has a similar form:⁹

$$F_{\text{Ne}^{9+}} = 0.2249 - 0.22609 \exp(-(N_{\text{O}^{7+}}/N_{\text{O}^{6+}} - 0.00094032)/6.9627)). \quad (2)$$

This empirical relation was required, as ACE did not measure Ne^{9+} at the time of the observations, so that abundance must be extrapolated from the contemporary oxygen ion abundance ratios that ACE did measure. These ion fluxes are calculated based on the $N_{\text{O}^{7+}}/N_{\text{O}^{6+}}$ ratio, which already takes into account the solar wind type (discussed below), and are then combined with the other parameters as described in Equation (1).

Two versions of the SWCX simulations were tested. In both cases, we assumed that the ions travel with the same velocity as the protons. In Model 1, we assumed a uniform slow solar wind ion flux distribution F_{Xq+} over all helioclitudes along the line of sight, with constant charge exchange cross sections $\sigma_{n,Xq+}$. Such an assumption approximates the existence of pseudostreamers and other sources of slow solar wind beyond the equatorial zone, as suggested in Yogesh et al. (2021). In Model 2, we assumed that the proton (and hence the ion) flux and velocity profiles are a function of helioclatitude. The proton flux (black solid curve in left panel of Figure 5; normalized to the equatorial value) and velocity profile (red dashed curve in left panel of Figure 5) were derived from a full-sky hydrogen Ly α map inversion analysis (Koutroumpa et al. 2019) based on data from the SWAN (Bertaux et al. 1988) instrument on board the Solar and Heliospheric Observatory (SOHO; Domingo et al. 1995). These

⁹ The three ion fluxes are calculated as $N_{Xq+} \times V$, where N_{Xq+} is in cm^{-3} and V is in km s^{-1} , and then fitted as a function of $N_{\text{O}^{7+}}/N_{\text{O}^{6+}}$. Therefore, the three empirical relations are in units of 10^5 particles $\text{cm}^{-2} \text{ s}^{-1}$.

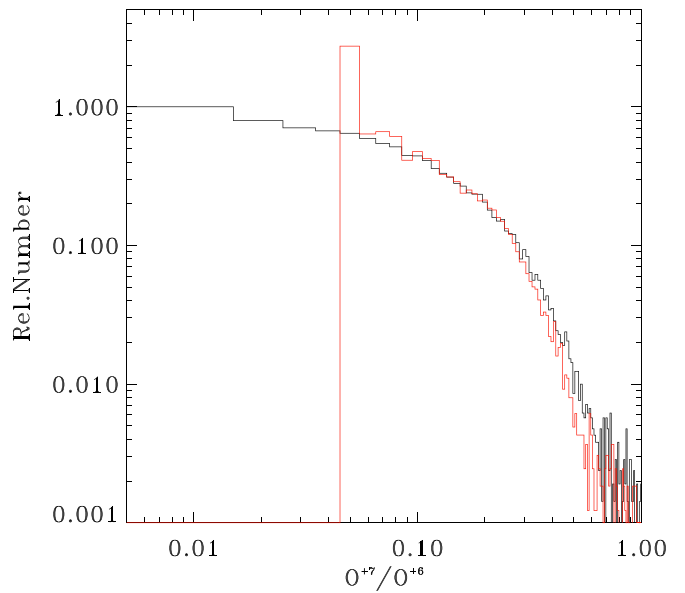


Figure 6. Histogram of $N_{\text{O}^{7+}}/N_{\text{O}^{6+}}$ with ratios from ACE. Black: before the ACE anomaly (1998–2011). Red: after the ACE anomaly (2011–2020). The figure is not adjusted for solar cycle.

profiles (henceforth called SWAN profiles) are employed in the heliospheric SWCX simulations in two ways: (1) the ion flux derived from ACE in-ecliptic data is adjusted to the SWAN relative flux profile according to the projected latitude on the line-of-sight step, and (2) the SWAN velocity profile is used to determine the charge exchange cross sections to be employed at that step from the velocity at that latitude.

It is well known that the “fast” and “slow” solar winds are better defined by their ion abundances than their speeds (see Section 3.1 of Kuntz 2018), but it is the solar wind speed, not the ion abundances, that affects the cross sections for charge exchange interactions. The division between fast and slow solar winds can be set at $\sim 550 \text{ km s}^{-1}$ (vertical lines in Figure 5). We have employed the simplifying assumption that we can characterize the cross section with only two values, one for the slow solar wind and one for the fast solar wind. The variation of the cross section with velocity is not sufficiently characterized for this assumption to introduce unnecessary uncertainties. The photon yield velocity dependence is very small between the slow and fast solar wind regimes and was not taken into account. The latitude-dependent simulations mainly impact the ESP, with a maximum factor of 1.6 ($I_{\text{Model 1}}/I_{\text{Model 2}}$) in the case of the Feb2020 observation, for which the velocity latitude profile is shown in the right panel of Figure 5. In this case, the fast solar wind regime influences most of the line of sight starting at ~ 1.2 au from the Sun.

One problematic factor in the model is the $N_{\text{O}^{7+}}/N_{\text{O}^{6+}}$ ratio in the empirical relations, which were used in both the heliospheric and later in the magnetospheric model calculations of the O VII line intensities (see Section 6.2). The empirical relations were derived using the complete ACE database through 2011 (~ 1998 –2011). In 2011 August, a radiation- and age-induced anomaly altered the ACE instrument, and a different data processing method was employed by the ACE team, producing a reduced set of solar wind parameters. The distribution of $N_{\text{O}^{7+}}/N_{\text{O}^{6+}}$ in the post-2011 data is rather different from the pre-2011 data, as shown in Figure 6. Although it is not clear how to relate the pre- and post-2011

Table 2
SWCX Model Parameters

Ion(s)	Energy (keV)	Ratio
S IX, N VI	0.4434	(Q)/(O VIIa) = 0.925
C VI, N VII		
O VIIa	0.5633	1.0
O VIIb	0.6792	(Q)/(O VIIa) = 0.126
O VIIIa	0.6531	1.0
O VIIIb	0.8031	(Q)/(O VIIIa) = 0.549
Ne IXa	0.9087	1.0
Ne IXb	1.1004	(Q)/(Ne IXa) = 0.100

Note. Primary ion lines are indicated with an “a” and secondary lines with a “b.” During spectral fitting, the low-energy line is either held fixed relative to O VIIa with the given ratio or fitted simultaneously with the other primary lines.

ratios in an absolute sense, the models for the two different fields observed will be affected in the same ways.

3.2. Heliospheric SWCX Spectrum

The two model versions presented predict the line intensities for each ion, namely O VII, O VIII, and Ne IX, but the energy positions of each ion line must be calculated separately. Here we choose to calculate the energy positions of each line instead of fitting for the values in the spectral fitting procedure, thus significantly reducing the number of fitted variables. We will find that the assumptions taken in the calculation prove to be inconsequential in the final result. Given HaloSat’s moderate energy resolution, emission lines within 80 eV from the same ion were combined using calculated line ratios, resulting in two emission lines for each ion. The known SWCX emission lines below 0.5 keV, a region where HaloSat has poor energy resolution, are not separable but do produce a pseudocontinuum and are combined in the same manner into the “low-energy SWCX line.”

The contributing ion species, calculated energy, and line ratio are given for each Gaussian in Table 2, with an assumed energy width of 0.001 keV. The primary lines for each ion are indicated with a unity ratio to the calculated values and an “a” in the ion column. The secondary lines are always held fixed relative to the ion’s primary line with the given ratio, while the primary lines may be either all fixed to the calculated line intensities or all fitted simultaneously, depending on the goal of the fitting process. When the primary lines are fixed, the low-energy line is also held fixed relative to the O VIIa calculated value. Otherwise, the low-energy line is fitted simultaneously with the other primary lines.

The line ratios were calculated assuming that all of the charge exchange interactions observed were due to the He neutrals, which dominate the observations of the He cone. This is further justified because the He cone enhancement spatially coincides with the H ionization cavity, where the interplanetary H density (and thus the SWCX emissivity due to H) is lowest due to the ionizing effects of the Sun on interstellar H atoms (see Figure 1). These line ratios were also used to weight the average energy position of the combined lines. Since this assumption also affects the position of the lines, we calculated the energies, assuming that the charge exchange interactions were 100% He and compared to the calculated values assuming 100% H. The energies of each combined line were different by

less than 6 eV in all cases, which is not resolvable in these data. The energy values assuming 100% He are given in Table 2.

3.3. Astrophysical and Particle Model

The astrophysical emission expected in both fields of view includes emission from the LHB, Galactic halo, and cosmic X-ray background (CXB) and was modeled using Xspec v12.10.1 (Arnaud 1996), which minimizes the differences between the data and the total model by changing the free parameters until the best fit is found. Non-X-ray emission (the particle background) was represented by a power-law component with free amplitudes and indices folded through a diagonal response modeled individually for each detector. In other words, we fitted for the particle background parameters for each detector simultaneously. We assumed that the astrophysical emission was constant between observations and the particle background was well modeled by the chosen method, as in Kaaret et al. (2020). The LHB was modeled using a thermal emission model of a collisional ionization equilibrium (CIE) plasma with solar metallicity, with the emission measure fixed to the calculated values for the two fields of view using Liu et al. (2017) after removal of the SWCX foreground and temperature fixed to the average value from the same work: 0.097 keV. (A plasma in CIE is often modeled in Xspec by the “apec” model (Foster et al. 2012) and commonly referred to as a thermal component.) Similarly, the CXB was represented by an absorbed power law with parameters fixed to the results in Cappelluti et al. (2017) obtained without removing sources. Photons emitted from objects in the CXB are partially absorbed by intervening Galactic and intergalactic material in a manner dependent upon the photon wavelength, which is appropriately modeled by applying an absorption factor to the representative spectral component. Other than the particle background parameters, all other parameters, fixed and free, were required to be identical for the three detectors’ spectra, which were always fitted simultaneously.

Both targets are somewhat close to the Galactic anticenter, so we might expect the Galactic halo emission to be near the virial temperature of ~ 0.2 keV. Thus, the Galactic halo was approximated with a single absorbed apec with temperature restricted to the range 0.1–0.35 keV with metallicity fixed to 0.3 solar (Miller & Bregman 2015; Kaaret et al. 2020). However, the ECL target is also close to the Galactic plane, making a significant X-ray contribution from young stellar objects more likely. In the case of the ECL target, the field of view barely covers the Taurus–Auriga molecular cloud complex at a distance of 140 pc, which is beyond the boundary of the LHB and possibly several interarm regions beyond the molecular cloud. The possibility of a significant contribution by these sources to the spectra is addressed in the next section and Section 5.

The absorption that must be applied to the Galactic halo and CXB was modeled with the “tbabs” model using the Wilms abundances (Wilms et al. 2000). Even though the bulk of the absorption is done by metals (anything other than hydrogen and helium), the input parameter is the total hydrogen nucleon column density, so the combined column density of hydrogen in all of its forms is included: molecular, neutral, and ionized. The ionized column is difficult to determine but is generally very small compared to the neutral column, especially over the large path length to the Galactic halo. The neutral column

density was determined from the 21 cm data of the HI4PI survey (HI4PI Collaboration 2016), which has a $16\prime.2$ beam. The H_2 column density was determined from the 1° beam $W_{\text{CO},J=1\rightarrow 0}$ map from Planck (Planck Collaboration 2014) and the conversion factor $X_{\text{CO}} = 2.0 \times 10^{20} \text{ H}_2 \text{ cm}^{-2} \text{ K}^{-1} \text{ km}^{-1} \text{ s}$. Since there is no way to directly survey the distribution of H_2 due to its lack of electric dipole transitions, we use the CO column density as a proxy and scale in the usual manner by the factor X_{CO} . In both cases, the beam size is much smaller than the HaloSat field of view, so there is no ambiguity about the column density measurements. There is, however, the usual uncertainty about the correct value for X_{CO} for these lines of sight, as well as the amount of H_2 not traced by CO.

4. Spectral Fitting

As sketched in the Introduction, we are taking a composite spectrum of each field separately, taken over many different observations with different SWCX strengths, and fitting all of the emission components simultaneously. Since the composite spectrum was obtained over many observations, it will contain an SWCX component that is roughly approximated by the mean SWCX model. Also, averaging over many observations averages over all of the abundance and ionization state variations. Thus, the SWCX model will be less sensitive to the uncertainties in these quantities.

We assume that our SWCX model for the composite spectrum is correct, fix its spectral shape and amplitude, and then fit for the Galactic halo and particle background components. This will produce our best estimate of the Galactic halo spectrum. As discussed earlier, spectral confusion between SWCX emission and astrophysical plasmas such as the Galactic halo is an issue, which is addressed through specialized spectral simulations described in this section. We will then use the final Galactic halo spectrum to isolate the variation in the SWCX spectrum in the individual observations, which we will then compare with that predicted by the heliospheric model. We will find that the spectra do not have sufficient signal-to-noise ratios to characterize the weaker SWCX lines; although we model all of the expected SWCX lines in our spectrum, we will characterize only the O VII line with significance. We apply the same method to both fields independently, as they contain very different astrophysical spectra and observe rather different solar winds.

4.1. The Composite Spectra

One composite spectrum for each target was generated separately using the best observations in each data set (bold observation names in Table 1). Given the large data set for the ECL target, observations with higher particle backgrounds or comparatively larger predicted O VII line intensities were excluded from the composite spectrum to reduce both noise due to the particle background and possible errors due to the slightly larger heliospheric SWCX emission in the spectrum. For this target, the observations included in the composite spectrum were Oct2018b, Nov2019a, Nov2019b, Nov2019c, and Oct2019. The same approach was not feasible for the ESP target due to the smaller number of successful observations. Instead, all low-background observations of the ESP were included in the composite spectrum (bold and italicized ESP observations in Table 1), regardless of the predicted O VII emission from heliospheric SWCX.

Each composite spectrum was used to model the halo emission in the associated field of view. For this step, the predicted heliospheric SWCX contribution using Model 2 was included as a fixed model component, and the best-fit parameters for the Galactic halo were acquired. (The CXB and LHB components were fixed and the particle backgrounds were fitted simultaneously, as described above.) In the ECL composite spectrum, the fitted temperature was pinned at the upper limit with characteristic broad residuals near 0.6 and 1 keV (Figure 7, left panel). The fitted temperature of the Galactic halo in the ESP composite spectrum was $0.280_{-0.013}^{+0.015}$ keV, which is somewhat high compared to the expected virial temperature of ~ 0.2 keV but not unreasonable given past measurements of the halo temperature (e.g., Nakashima et al. 2018; Kaaret et al. 2020). Since these works did not test for higher-temperature components, and the ECL fit showed clear large-scale residuals, a second absorbed thermal component was tested for both composite spectra.

As suspected, a second absorbed apec component with the same metallicity was well constrained for both spectra. Adding the higher-temperature component reduced the temperature of the warm-hot halo emission, thus contributing more emission at lower energies and reducing the residual feature previously seen at 0.6 keV (compare the left and right panels of Figure 7). The higher-temperature component ($kT \sim 1$ keV) contributes more emission at higher energies, similarly reducing the residual feature previously seen near 1.0 keV. Considering the higher-temperature emission primarily contributes above 0.7 keV, above the majority of the SWCX emission, it immediately follows that the higher-temperature component modeled should not be significantly affected by any changes in the SWCX emission, while the warm-hot halo emission is likely affected by such changes.

4.2. Spectral Simulation: SWCX versus Halo

Both the isotropic Model 1 and the solar wind latitudinal average profile we assumed in Model 2 depend on ACE's solar wind measurements in the ecliptic plane. Lack of in situ solar wind measurements along the high-latitude line of sight means that any changes in the solar wind toward higher latitudes cannot be included in the model unless the changes are recorded simultaneously by ACE at L1. Changes in the solar wind toward higher latitudes not recorded by ACE would produce some residual heliospheric SWCX not accounted for in the ESP spectra. However, higher-latitude changes in the solar wind are not likely to affect the majority of the ECL observations due to the large Sun angles and the low ecliptic latitude of the target.

The presence of undermodeled or overmodeled SWCX emission in the ESP composite spectrum should affect the warm-hot halo component in opposite manners. Undermodeled SWCX emission would leave an excess in the data as compared to the model at lower energies. Since the CXB and LHB components are fixed, this difference can only be compensated for by increasing the fitted warm-hot halo emission at lower energies, which results in a lower fitted temperature and a higher fitted amplitude. Similarly, overmodeled SWCX emission would result in more emission in the overall model than observed in the data at low energies. The spectral fitting process compensates for this difference by shifting the warm-hot halo emission to a higher temperature and lower amplitude, thus decreasing the amount of emission modeled at lower

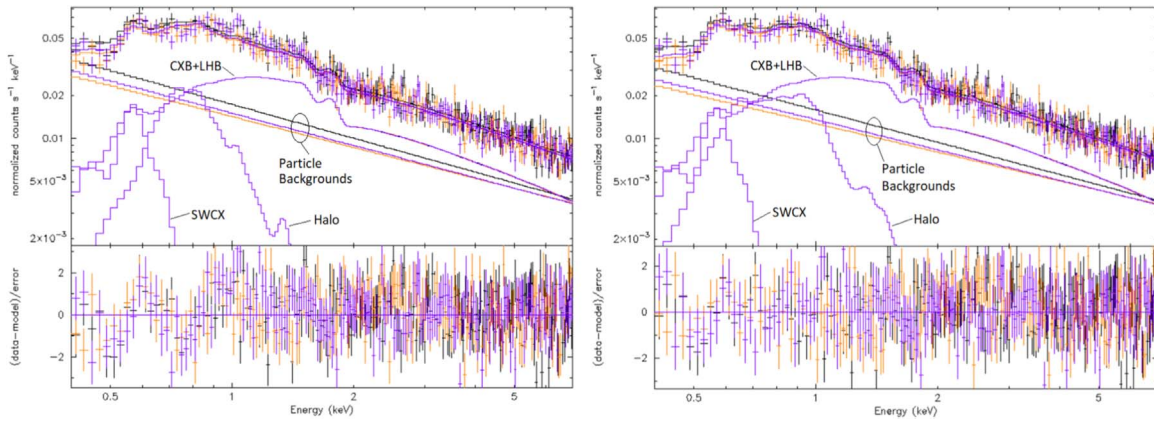


Figure 7. Initial spectral fits for ECL target composite spectrum. Left: using one absorbed apec component. Right: using two absorbed apec components. Both spectral fits were performed with the SWCX line intensities fixed to their calculated values using Model 2. Solid curves show the spectral components as labeled: heliospheric SWCX emission (SWCX; fixed), emission from the Galactic halo (Halo; fitted), emission from the CXB and LHB (CXB+LHB; fixed), the three particle backgrounds (straight lines; fitted), and the summed spectral model at the top. Crosses show the data as explained in the text; black, gold, and purple indicate detectors; and residuals are shown in the bottom panel. Note the broad residual features in the left panel near 0.6 and 1 keV indicating a poor fit when the Galactic halo is modeled with a single absorbed apec and the improvement in those residuals in the right panel when a second absorbed apec is added.

energies to better match the data observed. When the erroneous warm-hot halo parameters are then fixed while fitting the individual spectra, the resulting O VII line intensities are biased in the direction of the initial error. (Lower/higher fitted O VII line intensities result from undermodeled/overmodeled SWCX emission.)

To understand the extent of this “flux swapping” between the SWCX and the Galactic halo components, we tested the effect of changing the assumed SWCX fraction in the ECL spectra. We fitted the ECL composite spectrum with the Model 2 SWCX emission held fixed to the predicted values to obtain a set of Galactic halo parameters. Then, the composite ECL spectrum and the individual spectra used to generate it were simulated without the particle background and assuming the fitted Galactic halo parameters and Model 2 SWCX emission were correct. Finally, the resulting Galactic halo parameters were fixed in the spectral model while fitting the individual simulated spectra, and the SWCX line intensities were measured. This procedure was then repeated using SWCX line intensities scaled by $\pm 50\%$ in the spectral model as compared to the calculated values.

As suspected, the fitted parameters of the warm-hot Galactic halo component in the simulated composite spectral fit were significantly different compared to the initial values, but the higher-temperature parameter values were consistent (within the error bars). The temperature and emission measure of the warm-hot Galactic halo component were lower and higher, respectively, for the underestimation case (-50%), while the opposite trend occurred for the overestimation case ($+50\%$). Consequently, the fitted O VII line intensities in the simulated individual spectra, corresponding to the second stage of the actual analysis, were significantly lower than the simulated emission for the underestimation case, while no significant differences were observed in the overestimation case.

Interestingly, no changes in the residuals near the SWCX emission lines were noted in the spectra, meaning that flux at low energies can be ascribed to either the SWCX emission lines or the Galactic halo component without leaving a residual feature, which would indicate an error in the fitting. The only indication of properly modeled SWCX emission was a slightly lower χ^2_ν statistic for a unity scaling factor compared to the $\pm 50\%$ cases. In the actual spectra, residual SWCX emission

Table 3
Galactic Halo and SWCX Spectral Results

Description	ECL Values	ESP Values
l, b	$182^\circ 7, -16^\circ 4$	$271^\circ 2, -24^\circ 0$
$n_{\text{H}} (\times 10^{21} \text{ cm}^{-2})$	2.48	0.661
Warm-hot	$0.255^{+0.026}_{-0.024}$	$0.262^{+0.016}_{-0.014}$
Temperature (keV)		
Warm-hot	$9.2^{+1.8}_{-1.6}$	14.1 ± 1.6
Emission measure ^a		
Hot temperature (keV)	$1.01^{+0.13}_{-0.11}$	$1.03^{+0.23}_{-0.19}$
Hot emission measure ^a	$2.78^{+0.53}_{-0.54}$	$1.46^{+0.76}_{-0.75}$
Exposure (ks)	292.0	107.4
Degrees of freedom	566	300
χ^2_ν	1.099	1.017
Model 1 scaling factor (1σ)	$1.09^{+0.22}_{-0.27}$	$2.63^{+0.56}_{-0.61}$
Model 2 scaling factor (1σ)	$1.06^{+0.22}_{-0.26}$	$3.80^{+0.80}_{-0.88}$

Note.

^a Emission measure in units of $\times 10^{-3} \text{ cm}^{-6} \text{ pc}$. All errors are 90% confidence intervals unless otherwise noted. The Galactic halo temperatures and emission measures are reported with the SWCX scaling factor held fixed to the best-fit value. See text for more details.

can not only be shifted into the warm-hot Galactic halo component, as in the simulated case, but also possibly into the particle background.

5. Galactic Components

5.1. Results

Given that an assumed SWCX strength does modify the best-fit Galactic halo parameters, we may determine what SWCX strength leads to the best overall fit in the composite spectrum by determining the SWCX scaling factor that results in the lowest χ^2_ν statistic. We allowed the overall normalization of the Model 2 predicted SWCX spectrum, the “SWCX scaling factor,” to be fitted, with results given in Table 3. Presented in this table are the best-fit parameters with 90% confidence intervals for the Galactic halo emission in each field of view, corresponding Galactic coordinates, calculated hydrogen column densities, exposure times, fit statistics, and best-fit SWCX

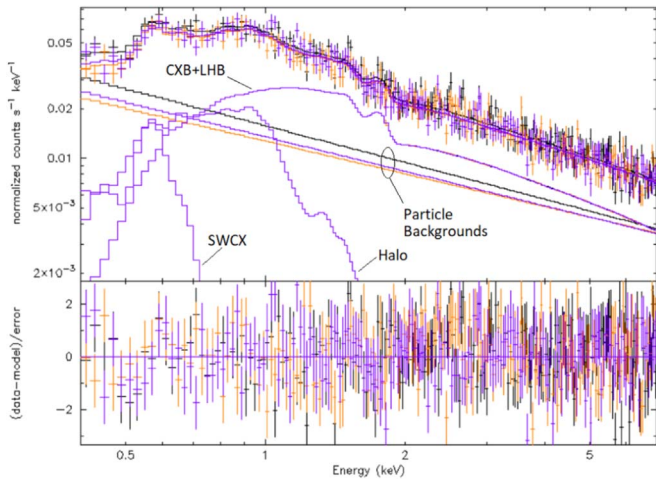


Figure 8. Spectral fit for ECL composite spectrum. The Model 2 SWCX line intensities were scaled by the best-fit factor (see text). Solid curves show the spectral components as labeled: heliospheric SWCX emission (SWCX; fixed), emission from the Galactic halo (Halo; fitted), emission from the CXB and LHB (CXB+LHB; fixed), the three particle backgrounds (straight lines; fitted), and the total spectral model at the top. Crosses show the data; black, gold, and purple indicate detectors; and residuals are shown in the bottom panel. The Ne IX SWCX contributions are not visible on this scale.

scaling factors with 1σ errors. The 90% confidence intervals are given with the SWCX scaling factor fixed to the best-fit value.

The SWCX scaling factor for each model and spectrum was derived by scaling the predicted line intensities by a range of values in a series of spectral fits. For each spectral fit, the SWCX scaling factor was fixed to a new value, while the Galactic halo and particle background parameters were fitted. The errors presented for the SWCX scaling factors were calculated by finding the best-fit SWCX scaling factor, calculating the $\Delta\chi^2$ for each spectral fit relative to the minimum value, interpolating the SWCX scale factor that would result in a $\Delta\chi^2$ of 2.706 between the two nearest spectral fits on both sides of the 90% confidence interval, and converting the resulting values to 1σ errors. As expected based on the spectral simulation described earlier, the fitted warm-hot Galactic halo temperatures and emission measures of the spectral fits closest to the $\Delta\chi^2 = 2.706$ boundaries for each target were not consistent, while the temperature and emission measure of the hot Galactic halo component were. The spectral fits for the best Model 2 SWCX scaling factors are plotted in Figures 8 and 9.

In the ECL field of view, the hot halo component is significantly detected by 8.5σ , while it is only marginally detected in the ESP field of view with a significance of 3.2σ . Comparing to a one-temperature Galactic halo model with the same SWCX scaling factors, the F-test probabilities for each are 6.7×10^{-14} and 6.5×10^{-3} for the ECL and ESP spectra. The F-test compares the number of degrees of freedom and the χ^2 of the two spectral models fitted separately to the same data set (for example, the ECL composite spectrum) and computes the probability that the additional additive component in the new model is warranted. The smaller the probability, the more likely that the additional component provides a better model of the emission and so should be kept in the spectral model. Since the F-test probabilities are quite low for the ECL spectrum when the higher-temperature component is added, and the amplitude of the higher-temperature component is significantly

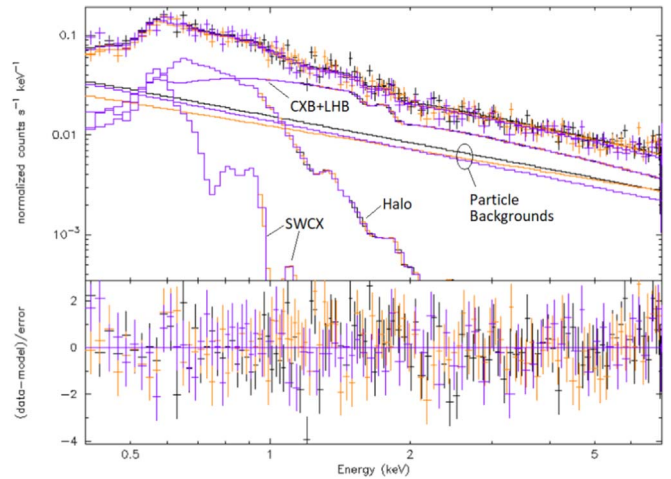


Figure 9. Spectral fit for the ESP composite spectrum. The Model 2 SWCX line intensities were scaled by the best-fit factor (see text). Solid curves show the spectral components as labeled: heliospheric SWCX emission (SWCX; fixed), emission from the Galactic halo (Halo; fitted), emission from the CXB and LHB (CXB+LHB; fixed), the three particle backgrounds (straight lines; fitted), and the total spectral model at the top. Crosses show the data; black, gold, and purple indicate detectors; and residuals are shown in the bottom panel.

above zero, we claim significant detection of a higher-temperature component in the ECL field of view. Similarly, we claim a marginally significant component of the same temperature in the ESP field of view. Notably, the ESP composite spectrum has about one-third of the exposure time of the ECL composite spectrum and a lower emission measure for the higher-temperature emission. Both factors limit the significance of the additional component in the ESP composite spectrum. More observing time for the ESP field of view in similar low-noise conditions would be needed to further test the significance of the higher-temperature component. Both spectra are discussed further in the next section.

Repeating the process using the Model 1 predictions converges to almost identical Galactic halo parameters for each field of view and so was not included in Table 3 to avoid repetition. The SWCX scaling factors for each target using Model 1 are also consistent with (within the error bars of) the corresponding values for the same targets using Model 2. Therefore, we cannot distinguish between the models for either the field of view near the ecliptic plane, where the predicted SWCX line intensities are consistent between the models, or at high ecliptic latitude, where the predicted line intensities of the two models are significantly different (see Table 4).

Considering the probable lack of magnetospheric SWCX emission in the ECL spectrum due to the large Sun angles, it is not surprising that the best-fit scaling factor is consistent with unity. Indeed, the differences between the right panel of Figure 7, where a unity SWCX scaling factor is used, and Figure 8, where the best-fit SWCX scaling factor is used, are quite small. On the other hand, the ESP observations were all taken through the magnetosheath. Thus, some portion of the additional SWCX emission observed may be magnetospheric, since we are observing through the flanks of the magnetosheath, while some portion could also be heliospheric SWCX resulting from fast changes in the solar wind at the higher ecliptic latitudes described earlier, which is not accounted for in the heliospheric SWCX model. The source of the excess emission is discussed further in Section 6.

Table 4
Comparison of Fitted and Predicted O VII Fluxes

Observation	Exposure (ks)	Fitted O VII (LU)	Model 1 Predicted O VII (LU)	Model 2 Predicted O VII (LU)	DoF	χ^2_ν	Satellite Ecliptic Longitude
Oct2018b	43.1	$1.49^{+0.27}_{-0.32}$	1.008 ± 0.042	1.036 ± 0.044	123	0.961	26°7
Nov2018a	29.3	$1.15^{+0.41}_{-0.47}$	1.240 ± 0.053	1.277 ± 0.054	122	1.113	52°1
<i>Nov2018b</i>	35.2	$1.20^{+0.43}_{-0.40}$	1.400 ± 0.054	1.442 ± 0.056	100	0.989	55°4
Sep2019	43.4	$0.65^{+0.36}_{-0.37}$	0.751 ± 0.031	0.773 ± 0.032	157	0.785	352°6
Oct2019	101.6	$0.98^{+0.20}_{-0.23}$	0.737 ± 0.053	0.759 ± 0.047	276	1.118	22°3
Nov2019	147.4	0.86 ± 0.18	1.105 ± 0.051	1.138 ± 0.053	353	0.978	52°0
<i>Dec2019</i>	266.2	0.82 ± 0.14	1.378 ± 0.063	1.420 ± 0.065	502	1.081	74°2
Mar2020	26.8	<0.46	0.814 ± 0.028	0.834 ± 0.029	89	1.000	160°0
Dec2018	154.8	$3.05^{+0.28}_{-0.27}$	1.461 ± 0.051	1.067 ± 0.038	470	1.113	74°9
<i>Dec2019a†</i>	24.7	$2.85^{+0.68}_{-0.67}$	1.567 ± 0.040	1.255 ± 0.032	139	0.894	72°1
Dec2019bc	34.7	$3.30^{+0.56}_{-0.53}$	1.295 ± 0.057	0.990 ± 0.052	149	1.058	75°1
Dec2019d	44.8	$1.89^{+0.40}_{-0.42}$	1.053 ± 0.059	0.688 ± 0.044	152	1.050	98°1
Feb2020	28.0	$2.42^{+0.63}_{-0.64}$	0.829 ± 0.028	0.514 ± 0.021	113	0.803	156°1

Note. Italicized observation names indicate observations with low backgrounds; bold observation names indicate observations used in the composite spectrum for each target. All errors are 1σ errors. LU = $\text{ph cm}^{-2} \text{s}^{-1} \text{sr}^{-1}$. Top: ECL results. Bottom: ESP results. The dagger indicates the ESP observation with a solar wind proton flux above the level chosen.

5.2. Discussion

The high-temperature component in the ECL composite spectrum could be explained by a large number of T Tauri stars near the Taurus cloud complex in the field of view (Wichmann et al. 1996; Güdel et al. 2007). (The T Tauri stars are pre-main-sequence stars known for high-temperature emission and prominent flaring.) However, Gaia DR2 data indicate only approximately 60 stars with estimated ages similar to typical T Tauri star ages (≤ 10 Myr) in the field of view (Luhman 2018; Kounkel & Covey 2019). Assuming an average T Tauri star flux and using the reported distances to the stars, the expected average X-ray flux from the young stars in the ECL field of view is $9.4 \times 10^{-12} \text{ erg cm}^{-2} \text{ s}^{-1}$, less than 1% of the observed flux from the high-temperature component. Thus, X-ray emission from these young stars does not account for the high-temperature emission observed. Comparatively, no stars younger than 10 Myr were reported in the Gaia DR2 data in the ESP field of view.

Another explanation for the high-temperature emission could be a contribution from dwarf M stars. However, the predicted emission from dwarf M stars falls rapidly with increasing Galactic latitude, with the majority of the emission predicted to be within 5° of the Galactic plane (Masui et al. 2009). In Yoshino et al. (2009), the dwarf M star emission model was unsuccessfully employed for an unexplained higher-temperature emission component in the LL10 spectrum, requiring an additional factor of 5 to represent the emission observed. Such a large scaling factor implies that an additional emission component was needed to explain the emission. In our case, both HaloSat fields of view were well outside of 5° of the Galactic plane, and our fitted higher temperatures were not consistent with the higher temperature of the dwarf M model ($0.766^{+0.039}_{-0.041} \text{ keV}$), so applying the dwarf M star emission model to our data was not justified.

Alternatively, Uprety et al. (2016) suggested a local interpretation for similar high-temperature emission. However, removing the absorption on the high-temperature component resulted in a poorer fit to the data, indicating a distant interpretation as more probable than a local one. Interestingly,

the fitted temperatures of the higher-temperature absorbed components in both fields of view were consistent with the value reported in Das et al. (2019b): $1.09^{+1.9}_{-0.64} \text{ keV}$ (90% CI) based on the Ne X absorption line but inconsistent with those reported in Das et al. (2019a) for emission. Although these two papers report a difference between absorption and emission temperatures for the same line of sight, other works report values in agreement for many sight lines, indicating that the emission and absorption temperatures are often consistent for other temperatures and lines of sight (Henley et al. 2010; Gupta et al. 2012, 2017). Thus, the small-amplitude high-temperature emission could possibly be from diffuse gas of $\approx 10^7 \text{ K}$ in the Galactic halo along the line of sight.

6. Performance of the Heliospheric Models

6.1. Results

Once the fitted parameters for the Galactic components in each field of view were obtained, the heliospheric SWCX contributions were measured in each individual observation by fixing the Galactic halo parameters for each target and fitting for the line intensities of the primary lines in Table 2 (including the low-energy line). Detection of SWCX emission in the spectral analysis depended on the total exposure time, the amplitude of the particle backgrounds, and the relative strength of the SWCX emission compared to all other sources. To improve the statistics, low-background observations of the same target occurring within a few days were combined, resulting in five low-background spectra for the ECL field and three low-background spectra for the ESP field. High-background observations were combined in a similar way; the observation with the high solar wind proton flux (Dec2019a) was kept separate. Spectral testing of observations with average count rates higher than $0.06 \text{ count s}^{-1}$ in the 3–7 keV band had difficulty resolving the O VII emission even for larger predicted O VII line intensities due to the additional noise in the spectra, so they are excluded from further analysis. The final set of spectra includes eight spectra for the ECL target and five spectra for the ESP. Table 4 lists the remaining observation names, exposure times, fitted O VII line intensities, predicted

O VII line intensities using Models 1 and 2, the spectral statistics of the fits, and the satellite’s ecliptic longitude for all spectra analyzed. All line intensities are given with 1σ errors. Results for the ECL target are given in the top portion of the table, with the ESP results given in the bottom.

Unfortunately, the fitted errors on the O VII line intensities dominate the errors in Table 4, even though the values are typically better than the required sensitivity of the 0.5 LU initially proposed for a 5 LU emission line. With the exception of the Dec2019 observation, all fitted O VII line intensities for the ECL observations were within 1.9σ and 1.8σ of the Model 2 and Model 1 predicted values, respectively. The Dec2019 observation was 4.0σ and 3.7σ lower than the Model 2 and Model 1 predicted line intensities. In contrast, the fitted O VII line intensities for the ESP observations were 2.8σ – 7.3σ above the Model 2 predictions and 2.0σ – 5.8σ above the Model 1 predictions. Interestingly, marginally significant excess emission from the low-energy SWCX emission line was observed only in the Dec2019bc ESP observation, 6.2σ higher than the model, with a line intensity 2.0σ above the expected value of 0.925 times the observed O VII line intensity. Finally, no significant detections of emission from O VIII or Ne IX in either spectral set were possible given the exposure times, the particle background levels, the relative weakness of these lines, and the low solar activity contributing to the observations.

6.2. Discussion

The fitted O VII line intensities in the ECL and ESP observations are plotted against the Model 1 and 2 predicted line intensities in Figure 10. Since the Model 1 and 2 predictions are within the models’ error bars for the ECL observations, the positions of the data markers are nearly identical in the two plots. On the other hand, the Model 2 predictions for the ESP observations are significantly smaller than the Model 1 predictions, shown by the horizontal shift of the ESP data to the right on the Model 1 plot (top panel) as compared to the Model 2 plot (bottom panel).

The solid lines in the two plots show where the measured O VII line intensities are equal to the predicted values. Data points below the lines indicate overprediction of the O VII line intensity, while data points above the lines show under-predicted values. The total χ^2/dof for this hypothesis for the ECL (ESP) observations is $4.930/8$ ($37.315/5$) and $5.352/8$ ($22.438/5$) for Models 1 and 2. Thus, we are unable to distinguish between the models for the ECL observations, which is not surprising, given that the Model 1 and 2 predictions are within the error bars. On the other hand, the Model 1 and 2 predictions for the ESP observations are distinct, and the comparison for the ESP observations strongly prefers the larger Model 1 predicted SWCX line intensities. The actual total χ^2 of the 1:1 hypothesis is likely larger due to probable underestimation of the errors in the predicted O VII intensities.

Interpreting possible excess emission in the ESP spectra as an offset yields fitted offsets of 1.45 ± 0.18 and 1.81 ± 0.18 LU (1σ) for Models 1 and 2 with 1σ errors taken into account during fitting, indicated by the red dashed lines in both panels. Alternatively, the ESP data trend could be interpreted as a steeper slope with zero offset, with fitted slopes of 1.67 ± 0.84 and 1.82 ± 0.84 for Models 1 and 2 (not shown), again accounting for 1σ errors during the fitting.

Given that the equatorial flow is strongly distinguished from the polar flow during solar minimum, and both flows are very

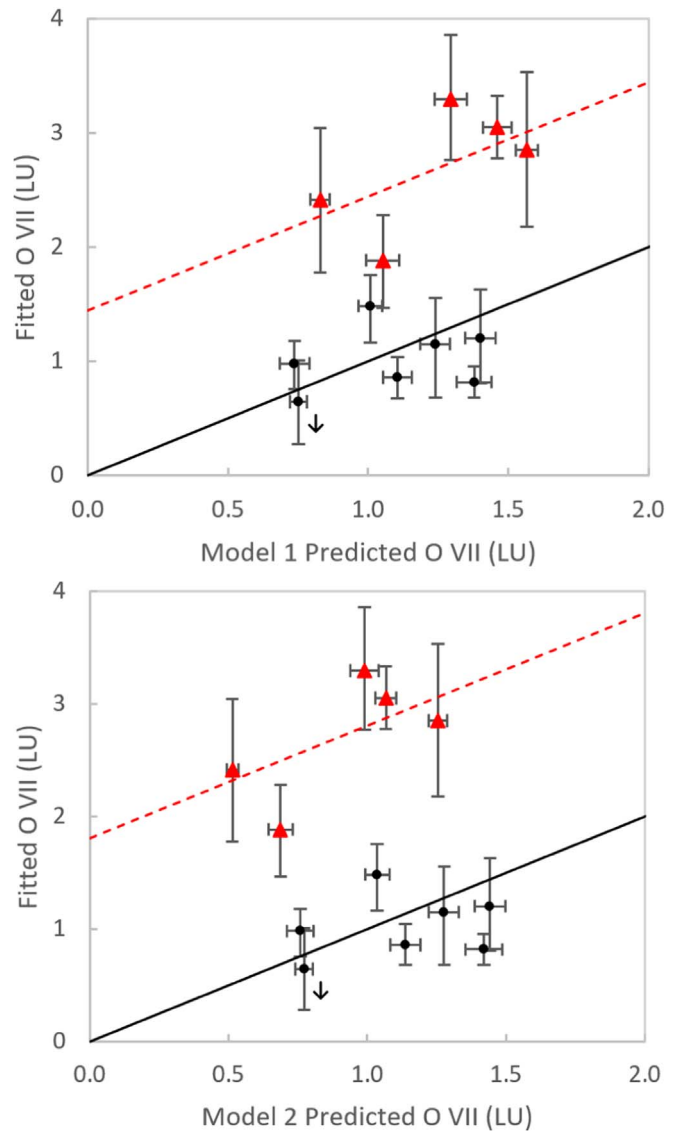


Figure 10. Measured vs. predicted O VII fluxes. Top: Model 1 predictions. Bottom: Model 2 predictions. The plotted values are given with 1σ errors. The ECL and ESP data are differentiated by the black circles and red triangles, respectively. The upper limit for the Mar2020 ECL observation is shown by the black arrow. The solid lines in each plot indicate a 1:1 relationship, and the dashed lines give a 1:1 relationship for the ESP data with a fitted offset from each model.

well defined in terms of abundances and ion ratios (Schwadron & Cravens 2000; von Steiger 2008), the observed O VII excess over the model in the ESP observations is very surprising. We have sought to find means to explain the observed excess without requiring additional heliospheric emission at high ecliptic latitudes. Two candidate sources for the O VII emission are explored in the following sections: magnetospheric SWCX emission and contamination by atmospheric O I emission.

6.2.1. Magnetospheric SWCX

The emission due to the heliosphere (Equation (1)) was given by the integral along the line of sight of the product of the ion flux, the neutral density, and the charge exchange cross section. Recasting the equation in terms of the proton flux, $F_P = N_P V_P$, and assuming the charge exchange interactions are predominantly with H in the exosphere yields the predicted

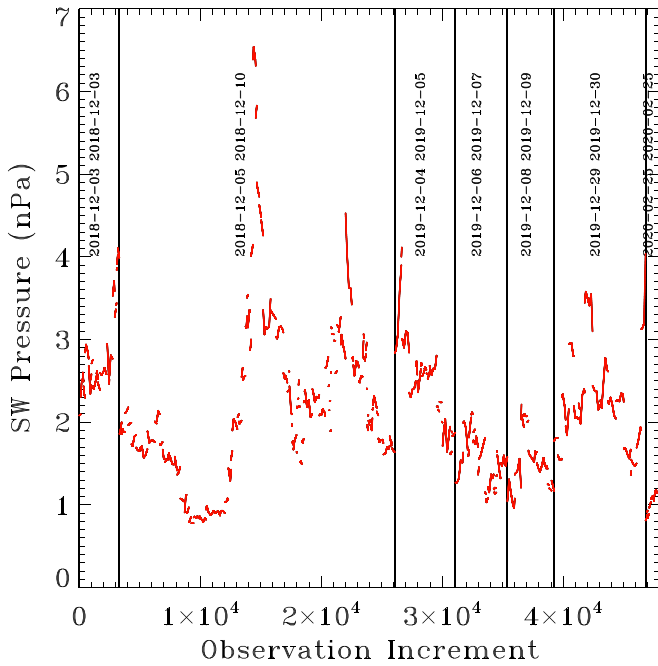


Figure 11. Solar wind pressure over the ESP observations from Table 1. From left to right, the date ranges correspond to the Dec2018a, Dec2018b, Dec2019a, Dec2019b, Dec2019c, Dec2019d, and Feb2020 ESP observations. The solar wind pressure was extracted from the 5 minute OMNI data.

X-ray line intensity in LU for O VII:

$$\begin{aligned}
 I &= \frac{1}{4\pi} \int_{\text{obs}}^{\infty} F_{O+7}(s) N_H(s) \sigma_{H,O+7} Y_{O\text{ VII},H} ds \\
 &= \frac{1}{4\pi} \frac{N_{O+7}}{N_p} \int_{\text{obs}}^{\infty} N_p(s) V_p(s) N_H(s) \sigma_{H,O+7} Y_{O\text{ VII},H} ds. \quad (3)
 \end{aligned}$$

In the magnetosheath, the situation is a bit more complex in that V_p is not just the bulk velocity but must include the thermal velocity as well: $V_p = \sqrt{(v_{\text{bulk}}^2 + v_{\text{therm}}^2)}$. Further, the proton density and velocity are strongly variable functions of location between the bow shock and the magnetopause due to the presence of the Earth’s magnetic field and are not directly measured but must be extracted from a MHD model. The neutral density due to the exosphere is rather uncertain and a matter of active research. We have used the model of Hodges (1994) out to $9.75 R_E$ and an r^{-3} extrapolation beyond that point. To determine N_{O+7}/N_p , we use the ACE SWICS 2.0 data to obtain N_{O+7}/N_{O+6} for each time period and then use the empirical relation given by Kaaret et al. (2020) to derive $N_{O+7}V$ from N_{O+7}/N_{O+6} , where V is the velocity of the free-flowing solar wind before it interacted with the Earth’s magnetic field. For time periods missing data, we have used the minimum measured N_{O+7}/N_{O+6} in the SS2 data.

The ESP observations were taken in seven segments, two in 2018 December, four in 2019 December, and a short one in 2020 February. As can be seen in Figure 11, the longest single segment by far is that taken on 2018 December 5–10 (Dec2018b), which also experienced the broadest range of solar wind pressures and thus the largest range of magnetosheath compression. In order to determine the magnetospheric contribution, we have acquired a BATS-R-US (Tóth et al. 2005) MHD simulation of the magnetosheath for each segment at a 20-minute cadence with the dipole tilt correctly tracked throughout the simulation. For each time step of the

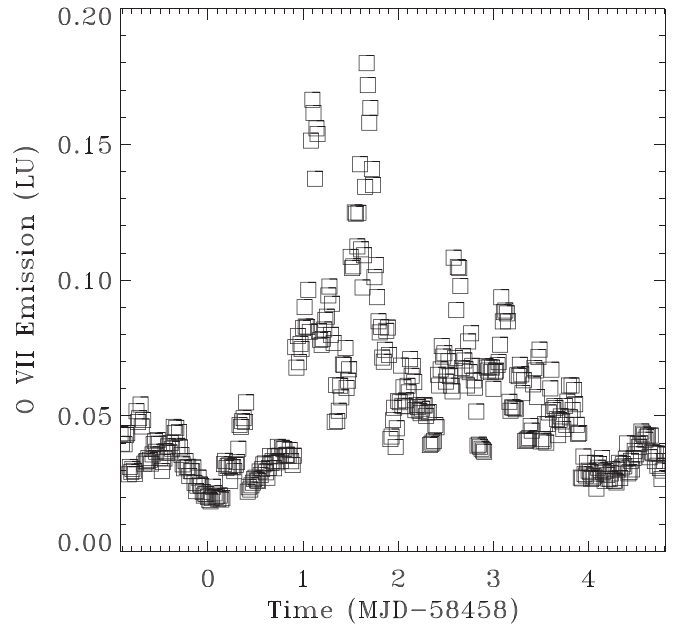


Figure 12. Emission in the O VII line due to magnetospheric emission for the ESP Dec2018b observation.

observations, we have sampled the MHD simulation for a line of sight from the spacecraft, through the magnetosheath, toward the ESP. We have taken the simplifying step of assuming that the spacecraft has $Z_{\text{GSE}} = 0$ and is at local midnight, assuming that the location in the orbit does not have a significant impact on the line-of-sight integrated emission. A comparison of the emission toward the ESP measured by the spacecraft at dawn and midnight in the Dec2018b simulation finds, on average, that $I_{\text{dawn}}/I_{\text{midnight}}$ averages to ~ 1.14 .

Figure 12 shows the expected O VII emission as a function of time from the MHD simulation of the 2018 December 5–10 (Dec2018b) observation segment. One can see that the line flux roughly follows the solar wind pressure and is typically less than a tenth of the observed value. This is not surprising. The typical value of Q for this spacecraft location and observing direction is $\sim 10^{19} \text{ cm}^{-4} \text{ s}^{-1}$ or less, with occasional excursions to larger values. From the SWICS data and the equation from Kaaret et al. (2020), the mean $N_{O+7} \sim 1.3 \times 10^{-4} \text{ cm}^{-3}$, which, combined with the OMNI proton density data, yields a mean $N_{O+7}/N_p \sim 3.0 \times 10^{-5}$. Thus, we get an average X-ray flux for this observation of 0.0511 LU in the O VII line. Similarly, the average X-ray fluxes resulting from independent simulations for the Dec2018, Dec2019a, Dec2019bc, Dec2019d, and Feb2020 ESP observations are 0.0494, 0.0768, 0.0560, 0.0311, and 0.0222 LU, where the results from each simulation were combined as in Table 4.

Interestingly, none of these expected contributions account for a significant portion of the emission detected and are much smaller than the fitted errors on the O VII line for the observations. As noted in Slavin et al. (2013) for similar observations of the He cone, the modeled magnetospheric SWCX emission is much weaker than the predicted heliospheric SWCX emission for these lines of sight through the flanks of the magnetosheath, and it is only a few percent of the heliospheric SWCX emission. Apart from the modeled heliospheric and magnetospheric contributions, approximately 0.8–2.0 LU of O VII line emission is not accounted for in the

individual observations, which is of the same order as the heliospheric SWCX initially predicted.

6.2.2. Atmospheric Contamination

Alternatively, the excess emission in the O VII line could result from atmospheric contamination. Due to the low altitude of HaloSat's orbit, observations taken through the magnetosheath have an increased possibility of contamination by neutral oxygen from the Earth's sunlit atmosphere along the line of sight, which is 38.3 eV from the primary O VII line (Table 2) and thus difficult to distinguish from O VII emission given HaloSat's moderate spectral resolution. Suzaku observations are known to have a similar contamination, also due to the instrument's low altitude, particularly for small elevation angles from the Earth's limb (Ezoe et al. 2011). Further analysis of the spectral contamination from neutral oxygen in Suzaku spectra postulated that increased O I emission for similar elevation angles in later spectra was due to increased solar activity, resulting in atmospheric expansion, as the solar cycle approached solar maximum (Sekiya et al. 2014). Given the variability of solar activity, this explanation also accounted for the lack of such emission in some observations in the same time period.

Similar contamination in HaloSat's ESP observations at solar minimum could explain the emission observed. Residual O I contamination of ≤ 2 LU was seen in Suzaku spectra, even at solar minimum (Sekiya et al. 2014). For the observations used in the ESP composite spectrum considered here, the smallest angle between the instrument pointing and the bright Earth limb was $67^\circ 0$. While this minimum is above the 60° minimum used to successfully remove the O I contamination in the Suzaku spectra, HaloSat's lower altitude and larger field of view act to increase the separation angle needed. However, removing all data from the composite ESP spectrum with bright Earth limb angles less than 175° , a total of 19.8 ks exposure time, failed to reduce the best-fit SWCX scaling factor in the ESP composite spectrum. In comparison, the smallest angle between the instrument pointing and the bright Earth limb during the ECL observations used for the composite spectrum was $86^\circ 8$, and no significant excess emission was found for those observations.

Additional spectral tests were performed in search of O I emission. Using the simulated composite ECL spectrum described in Section 4, which contains no O I, we added a Gaussian at 525 eV to the fitted model for SWCX scaling factors of 1, 0.5, and 1.5. The resulting O I line intensity of each spectral fit was either equal to or consistent with zero. We also tested for O I contamination in the actual composite ESP spectrum by adding a Gaussian line at 525 keV to the fitted model. For both the best-fit SWCX scaling factor (from Table 3) and a unity scaling factor, the line intensity of the O I line was pegged at zero during the analysis process using Model 2 without successful completion. Similar results are expected using Model 1.

Finally, the composite ESP spectrum was simulated to test whether O I contamination would produce the high SWCX scaling factor observed in the data. As done for the ECL composite spectrum in Section 4, the ESP composite spectrum was simulated without the particle background, assuming the Model 2 SWCX line intensities were accurate, using the X-ray parameters reported in Table 3 and described in Section 3 and adding a Gaussian representing O I contamination at 525 eV

with an energy width of 0.001 eV and a line intensity equal to the fitted offset of ~ 1.8 LU for Model 2. The simulated spectrum was then modeled with fixed SWCX scaling factors ranging from zero to four while fitting for the Galactic components. No Gaussian for O I was included in the model fitted to the simulated spectrum.

The best-fit SWCX scaling factor for the ESP simulated composite spectrum was zero with an upper limit of 1.3 (90% CI). Also, residual excesses at the O I energy were observed in all spectral fits. This simulation result indicates that if O I contamination were present in the actual ESP composite spectrum, then we would expect a smaller best-fit SWCX scaling factor with residual excesses at the O I energy. However, the actual ESP SWCX scaling factor is higher than expected, and no residual excesses are noted in either of the actual spectra near 525 eV. Thus, spectral simulations and tests fail to detect O I in the ESP composite spectrum.

6.2.3. Heliospheric SWCX

The previous two sections have shown that the excess O VII emission in the ESP field is not due to either magnetospheric SWCX or atmospheric contamination. We must conclude that the models of the emission at high latitude are not yet complete, or there is some physics we do not yet understand. One possible explanation is additional heliospheric SWCX emission due to the solar wind distribution, which is difficult to model for the ESP spectra, since it is not currently monitored at high latitudes. A similar difference in modeled emission between low and high ecliptic observations has been seen with other missions (see Figures 25 and 26 of Kuntz 2018 for an example; Koutroumpa et al., private communication).

In order for the high-latitude heliospheric SWCX signal to account for the excess emission, the solar wind oxygen content needs to amount to twice as much as the values measured at L1. Such extreme changes in solar wind composition are usually associated with interplanetary coronal mass ejections (ICMEs), where the oxygen content may increase even by a factor of 10 (Richardson & Cane 2010). Although no particular event can be directly linked to our observations, there are some indications of increased CME activity in the southern hemisphere both in 2018 December and 2019 December according to the SECCHI/C2 and LASCO/C2 coronagraph difference images.¹⁰ The increased CME frequency may have enriched the southern hemisphere in highly charged ions, which could have produced the enhanced SWCX signal.

6.2.4. He Cone Signature

We now turn to discuss an important result based on the ECL observations taken by HaloSat at solar minimum. For the ECL observations in 2019, there was a slight increasing trend for the observed O VII intensities with the satellite ecliptic longitude for both targets. The trend also exhibited a local maximum when the observer position was close the He cone axis in December (when maximum emission is expected). However, the values are within the 1σ error bars. Since the fitted O VII line intensities in each set are within the errors, we do not detect the spatial signature of the He cone at solar minimum in the oxygen lines' energy range. Given that the Model 1 and 2 predictions for the ECL observations are also

¹⁰ <http://spaceweather.gmu.edu/seeds/>

within the observational error bars (~ 0.4 LU for each), this is not surprising. These observations were not designed to measure the size of the He cone but rather the temporal variability due to the solar wind. Repeating these observations at solar maximum, when strong variations of solar wind strength are more likely, would yield more distinguishable measurements for the observed solar wind conditions. If a much larger collection area is used, then an attempt to measure the size of the He cone would also be possible.

6.2.5. Concluding Remarks

As mentioned earlier, the SWCX model calculations depend on the helium–oxygen cross section, the ion fluxes, the line emissivities, and, additionally, the solar wind profiles for Model 2. So, we can only conclude that the combination of the values is slightly larger than but consistent with those predicted in the ECL observations. For the ESP observations, we report 0.8–2.0 LU of O VII emission in excess of model predictions, evident as either steeper slopes, as in Kuntz (2018), or as an offset for the ESP data, as shown in Figure 10, which is likely heliospheric SWCX emission caused by the solar wind distribution at high ecliptic latitudes not accounted for by our heliospheric SWCX emission models. The excess emission is indicated by the marginally higher SWCX scaling factor obtained when fitting the ESP composite spectrum. The excesses in the individual ESP spectra follow from that scaling factor. However, none of the individual observations show significant deviations from this excess, including the observation with a slightly high solar wind proton flux; the excess found in the composite spectrum was not due to a single aberrant observation. Also, the errors in the predicted O VII intensities are likely underestimated, which further reduces the significance of the differences between the measured and predicted values. Consequently, we regard the excess O VII emission observed as concerning but not problematic. Additional high-quality observations of the ESP will better constrain the warm–hot halo and SWCX emission components, possibly resolving this issue.

7. Summary

The list below briefly outlines the results of this work and is followed by a more detailed discussion.

1. We do not distinguish between a heliolatitude-dependent solar wind profile and an isotropic profile based on SWCX emission observed near solar minimum.
2. We do not significantly detect the predicted heliospheric SWCX variations of the He cone during two transits of the He cone near solar minimum.
3. We observe an excess of 0.8–2.0 LU of O VII line emission in the direction of the ESP, which is not explained by modeled heliospheric or magnetospheric SWCX emission or atmospheric contamination.
4. We report fitted spectral parameters for the astrophysical emission in both fields of view after careful, time-dependent modeling of the heliospheric SWCX emission in each observation.
5. We detect ~ 1 keV absorbed thermal emission in both fields of view examined in this study.

We report on a series of X-ray observations through the He cone with moderate spectral resolution. Using these

observations, we evaluated the performance of a heliospheric SWCX emission model with updated neutral distributions and solar wind parameters. Spectral modeling indicated that we can only separate the Galactic halo components from SWCX emission by searching for the best-fit SWCX scaling factor. Based on the best-fit SWCX scaling factors for a combination of the best observations of each target (Table 3), we cannot significantly distinguish between Model 2, which assumes a heliolatitude-dependent solar wind profile, and Model 1, which assumes an isotropic slow solar wind, for the two fields of view.

With the Galactic components fixed, we also compared the model predictions and observed SWCX emission for the series of observations. The two models were indistinguishable in the ecliptic plane and predicted ~ 0.6 LU enhancement for O VII when looking straight down the He cone. Although the data could not distinguish the predicted heliospheric SWCX variations of the He cone, the average level of SWCX in the ECL field agreed with the models. For the ESP observations, heliospheric and magnetospheric SWCX models and atmospheric contamination failed to account for 0.8–2.0 LU of O VII line emission, which is possibly due to heliospheric emission at high ecliptic latitudes not predicted by our models. Additional simultaneous observations in the ecliptic plane and roughly toward the ecliptic poles, preferably during transits of the He cone, are imperative to further investigate this discrepancy. Curiously, ~ 1 keV absorbed thermal emission was detected in both fields of view, consistent with the Ne X absorption line measurement in Das et al. (2019b).










Improved results are possible with additional X-ray observations during transits of the He cone closer to solar maximum, when the Sun is typically more active, and thus more heliospheric SWCX emission is expected. In the future, the final Galactic parameter values reported in Table 3 can be used to independently constrain the astrophysical background emission in other measurements of SWCX emission for the two fields of view observed.

The processing files used in this analysis are available online through HEASARC’s archive. As of the date of this writing, data from the HaloSat mission are available through the same website through 2019 October 15. The remaining data are scheduled to be available in 2021 July, which is 6 months after the instrument reentered the atmosphere in 2021 January.

The authors acknowledge the use of SWICS data provided by the ACE Science Center (<http://www.srl.caltech.edu/ACE/ASC/>) and especially wish to extend their thanks to Jim Raines for endless discussions on the data. The authors also acknowledge the use of OMNI data provided by NASA/GSFC’s Space Physics Data Facility’s OMNIWeb service and magnetospheric simulation results from the Community Coordinated Modeling Center at Goddard Space Flight Center. The CCMC is a multiagency partnership between NASA, AFMC, AFOSR, AFRL, AFWA, NOAA, NSF, and ONR. The SWMF/BATS-RUS model was developed by Tamas Gombosi et al. at the Center for Space Environment Modeling, University of Michigan. The authors also acknowledge helpful comments from E. Hodges-Kluck. The HaloSat mission is supported by NASA grant NNX15AU57G. A portion of R.R.’s work was supported by ADNET Systems, Inc. D.K.’s modeling work was supported by CNES and performed with the High

Performance Computer and Visualisation platform (HPCaVe) hosted by UPMC-Sorbonne Université.

ORCID iDs

R. Ringuette  <https://orcid.org/0000-0003-0875-2023>
 D. Koutroumpa  <https://orcid.org/0000-0002-5716-3412>
 K. D. Kuntz  <https://orcid.org/0000-0001-6654-5378>
 P. Kaaret  <https://orcid.org/0000-0002-3638-0637>
 K. Jahoda  <https://orcid.org/0000-0003-0100-6415>
 D. LaRocca  <https://orcid.org/0000-0002-7529-4619>
 M. Kounkel  <https://orcid.org/0000-0002-5365-1267>
 J. Richardson  <https://orcid.org/0000-0001-8138-7582>
 J. Bluem  <https://orcid.org/0000-0001-8307-7166>

References

- Arnaud, K. A. 1996, in ASP Conf. Ser. 101, *Astronomical Data Analysis Software and Systems V*, ed. G. H. Jacoby & J. Barnes (San Francisco, CA: ASP), 17
- Bertaux, J. L., Lallement, R., Kurt, V. G., & Mironova, E. N. 1985, *A&A*, 150, 1
- Bertaux, J. L., Pellinen, R., Chassefiere, E., et al. 1988, *The SOHO Mission. Scientific and Technical Aspects of the Instruments* (Noordwijk: ESA), 63
- Bertaux, J. L., Quémerais, E., Lallement, R., et al. 1997, *SoPh*, 175, 737
- Burlaga, L. F., Ness, N. F., Belcher, J. W., Lazarus, A. J., & Richardson, J. D. 1996, *SSRv*, 78, 33
- Bzowski, M. 2008, *A&A*, 488, 1057
- Cappelluti, N., Li, Y., Ricarte, A., et al. 2017, *ApJ*, 837, 19
- Collaboration, H. 2016, *A&A*, 594, A116
- Collaboration, P. 2014, *A&A*, 571, A13
- Cox, D. P. 1998, in IAU Coll. 166, *The Local Bubble and Beyond*, ed. D. Breitschwerdt, M. J. Freyberg, & J. Truemper (Berlin: Springer), 121
- Cravens, T. E. 1997, *GeoRL*, 24, 105
- Cravens, T. E., Robertson, I. P., & Snowden, S. L. 2001, *JGR*, 106, 24883
- Czechowski, A., Hilchenbach, M., & Kallenbach, R. 2006, *ISSIR*, 5, 311
- Czechowski, A., Hsieh, K. C., Hilchenbach, M., Kota, J., & Shaw, A. W. 2004, *AdSpR*, 34, 104
- Dalaudier, F., Bertaux, J. L., Kurt, V. G., & Mironova, E. N. 1984, *A&A*, 134, 171
- Das, S., Mathur, S., Gupta, A., Nicastro, F., & Krongold, Y. 2019a, *ApJ*, 887, 257
- Das, S., Mathur, S., Nicastro, F., & Krongold, Y. 2019b, *ApJ*, 882, L23
- Domingo, V., Fleck, B., & Poland, A. I. 1995, *SSRv*, 72, 81
- Ezoe, Y., Miyoshi, Y., Yoshitake, H., et al. 2011, *PASJ*, 63, S691
- Fahr, H. J. 1968, *Ap&SS*, 2, 474
- Foster, A. R., Ji, L., Smith, R. K., & Brickhouse, N. S. 2012, *ApJ*, 756, 128
- Freyberg, M. J. 1994, PhD thesis, Technische Univ. München
- Freyberg, M. J. 1998, in IAU Colloq. 166, *The Local Bubble and Beyond*, ed. D. Breitschwerdt, M. J. Freyberg, & J. Truemper (Berlin: Springer), 113
- Galeazzi, M., Chiao, M., Collier, M. R., et al. 2014, *Natur*, 512, 171
- Gloeckler, G. 1996, *SSRv*, 78, 335
- Gloeckler, G., Cain, J., Ipavich, F. M., et al. 1998, *The Advanced Composition Explorer Mission* (Netherlands: Springer), 497
- Güdel, M., Briggs, K. R., Arzner, K., et al. 2007, *A&A*, 468, 353
- Gupta, A., Mathur, S., & Krongold, Y. 2017, *ApJ*, 836, 243
- Gupta, A., Mathur, S., Krongold, Y., Nicastro, F., & Galeazzi, M. 2012, *ApJ*, 756, L8
- Henley, D. B., Shelton, R. L., Kwak, K., Joung, M. R., & Low, M.-M. M. 2010, *ApJ*, 723, 935
- Hilchenbach, M., Hsieh, K. C., Hovestadt, D., et al. 1998, *ApJ*, 503, 916
- Hodges, R. R. 1994, *JGR*, 99, 23229
- Kaaret, P., Koutroumpa, D., Kuntz, K., et al. 2020, *NatAs*, 4, 1072
- Kaaret, P., Zajczyk, A., LaRocca, D. M., et al. 2019, *ApJ*, 884, 162
- Katushkina, O. A., & Izmodenov, V. V. 2010, *AstL*, 36, 297
- King, J. H., & Papitashvili, N. E. 2005, *JGRA*, 110, A02104
- Kounkel, M., & Covey, K. 2019, *AJ*, 158, 122
- Koutroumpa, D. 2012, *AN*, 333, 341
- Koutroumpa, D., Acero, F., Lallement, R., Ballet, J., & Kharchenko, V. 2007, *A&A*, 475, 901
- Koutroumpa, D., Collier, M. R., Kuntz, K. D., Lallement, R., & Snowden, S. L. 2009, *ApJ*, 697, 1214
- Koutroumpa, D., Lallement, R., Kharchenko, V., et al. 2006, *A&A*, 460, 289
- Koutroumpa, D., Quémerais, E., Ferron, S., & Schmidt, W. 2019, *GeoRL*, 46, 4114
- Kuntz, K. D. 2018, *A&ARv*, 27, 1
- Lallement, R., Bertaux, J. L., & Dalaudier, F. 1985, *A&A*, 150, 21
- Lallement, R., Raymond, J. C., Vallerger, J., et al. 2004, *A&A*, 426, 875
- LaRocca, D. M., Kaaret, P., Kirchner, D. L., et al. 2020, *JATIS*, 6, 014003
- Lisse, C. M., Dennerl, K., Englhauser, J., et al. 1996, *Sci*, 274, 205
- Liu, W., Chiao, M., Collier, M. R., et al. 2017, *ApJ*, 834, 33
- Luhman, K. L. 2018, *AJ*, 156, 271
- Masui, K., Mitsuda, K., Yamasaki, N. Y., et al. 2009, *PASJ*, 61, S115
- Miller, M. J., & Bregman, J. N. 2015, *ApJ*, 800, 14
- Möbius, E., Bzowski, M., Chalov, S., et al. 2004, *A&A*, 426, 897
- Möbius, E., Hovestadt, D., Klecker, B., et al. 1985, *Natur*, 318, 426
- Nakashima, S., Inoue, Y., Yamasaki, N., et al. 2018, *ApJ*, 862, 34
- Quémerais, E., Bertaux, J.-L., Lallement, R., et al. 1999, *JGR*, 104, 12585
- Richardson, I. G., & Cane, H. V. 2010, *SoPh*, 264, 189
- Schmitt, J. H. M. M., Snowden, S. L., Aschenbach, B., et al. 1991, *Natur*, 349, 583
- Schwadron, N. A., & Cravens, T. E. 2000, *ApJ*, 544, 558
- Schwadron, N. A., & McComas, D. J. 2010, *ApJL*, 712, L157
- Sekiya, N., Yamasaki, N. Y., Mitsuda, K., & Takei, Y. 2014, *PASJ*, 66, L3
- Slavin, J. D., Wargelin, B. J., & Koutroumpa, D. 2013, *ApJ*, 779, 13
- Sokół, J. M., McComas, D. J., Bzowski, M., & Tokumaru, M. 2020, *ApJ*, 897, 179
- Tóth, G., Sokolov, I. V., Gombosi, T. I., et al. 2005, *JGRA*, 110, A12226
- Uprey, Y., Chiao, M., Collier, M. R., et al. 2016, *ApJ*, 829, 83
- von Steiger, R. 2008, *The Heliosphere through the Solar Activity Cycle* (Berlin: Springer), 41
- Wichmann, R., Krautter, J., Schmitt, J. H. M. M., et al. 1996, *A&A*, 312, 439
- Wilms, J., Allen, A., & McCray, R. 2000, *ApJ*, 542, 914
- Witte, M., Banaszekiewicz, M., & Rosenbauer, H. 1996, *SSRv*, 78, 289
- Yogesh, Chakrabarty, D., & Srivastava, N. 2021, *MNRAS*, 503, L17
- Yoshino, T., Mitsuda, K., Yamasaki, N. Y., et al. 2009, *PASJ*, 61, 805
- Zajczyk, A., Kaaret, P., LaRocca, D., et al. 2020, *JATIS*, 6, 044005